Journal of
Materials Chemistry B

Materials for biology and medicine

Accepted Manuscript

Published on 24 August 2026

This is an Accepted Manuscript, which has been through the Royal Society of Chemistry peer review process and has been accepted for publication.

Accepted Manuscripts are published online shortly after acceptance, before technical editing, formatting and proof reading. Using this free service, authors can make their results available to the community, in citable form, before we publish the edited article. We will replace this Accepted Manuscript with the edited and formatted Advance Article as soon as it is available.

You can find more information about Accepted Manuscripts in the Information for Authors.

Please note that technical editing may introduce minor changes to the text and/or graphics, which may alter content. The journal's standard Terms & Conditions and the Ethical guidelines still apply. In no event shall the Royal Society of Chemistry be held responsible for any errors or omissions in this Accepted Manuscript or any consequences arising from the use of any information it contains.

ROYAL SOCIETY OF CHEMISTRY

rsc.li/materials-b

Silk Fibroin Nanoparticles Coated with Secretome-Derived Extracellular Vesicles via GMP-Ready Microfluidics: A Biomimetic Carrier-in-Carrier Platform with Preferential Tumor Cell Internalization

Edoardo Bertania[1§], Angelo Modena[1§], Elia Bari[1*], Ivana Miletto[1], Dmitry Lim[1], Lorena Segale[1], Giada Diana[1], Alessandro Candiani[1], Marzio Sorlini[2,3], and Maria Luisa Torre[1,2]

[1] Department of Pharmaceutical Sciences, University of Piemonte Orientale, Largo Donegani 2, 28100 Novara, Italy

[2] PharmaExceed S.r.l, Piazza Castello 19, 27100, Pavia, Italy

[3] Department of Innovative Technologies, University of Applied Sciences and Arts of Southern Switzerland, SUPSI, Lugano University Center, Campus Est, Via la Santa 1, CH-6962 Viganello, Switzerland

*correspondence: elia.bari@uniupo.it

§ These authors equally contributed

Abstract

The integration of synthetic nanocarriers with biologically derived membranes represents a promising strategy to engineer biomimetic systems for precision medicine. Here, we report a hybrid nanoplatform in which silk fibroin nanoparticles (SFNs) are coated with the vesicular fraction of a GMP-compliant lyosecretome (herein referred to as secretome-derived EVs), in a hierarchical carrier-in-carrier architecture, enabling the combination of tunable material properties with intrinsic biological functionality. A key advancement of this work is the development of a microfluidic, GMP-compatible assembly process that allows controlled and scalable production of secretome-derived EV-coated nanoparticles, addressing a major translational bottleneck in the field. The resulting hybrid nanostructures were characterized by nanoparticle tracking analysis and Förster resonance energy transfer, confirming nanoscale proximity between SFN surfaces and EV membranes consistent with EV membrane association. Using a model lipophilic compound, we demonstrate that EV-membrane association enhances colloidal stability, protects the payload from degradation, and enables sustained release profiles. Importantly, the biological identity of the secretome-derived EV membrane was found to modulate cellular interactions: EVs derived from mesenchymal stromal cells promoted preferential uptake in healthy cells, whereas tumor-derived EVs drove selective internalization in homologous cancer cells in vitro. These findings establish EV-coated SFNs as a versatile biomimetic

platform with programmable cell-type-specific uptake properties and scalable manufacturability, providing a foundation for the development of next-generation nanotherapeutics that integrate material design with biological specificity for precision oncology.

Keywords

Extracellular vesicles; silk fibroin nanoparticles; carrier-in-carrier drug delivery system; targeted drug delivery; microfluidics; precision oncology.

Acknowledgements

The authors thank Prof. Laura Moro and Prof. Giulia Pinton (Department of Pharmaceutical Sciences, University of Piemonte Orientale) for kindly providing mesothelioma cell lines. The authors also acknowledge Dr. Simone Reano (Core Facilities, University of Piemonte Orientale) for technical support with the two-photon confocal microscopy.

Funding

This work is part of the project RESALE, which has received funding from the European Commission - NextGeneration EU and Compagnia di San Paolo.

1. Introduction

In recent years, the development of precision drug delivery systems has become a central focus in biomedical research, aiming to transport therapeutic molecules specifically to diseased tissues while minimizing off-target accumulation and systemic toxicity [1]. This is particularly crucial in diseases such as cancer, where highly cytotoxic drugs require precise targeting to mitigate side effects [2-4]. Precision oncology further emphasizes the need for advanced delivery platforms capable of selectively targeting tumor cells while sparing healthy tissues, a goal increasingly addressed by nanotechnology through nanocarriers exploiting active, passive, and physical targeting mechanisms [5,6]. Among these, extracellular vesicles (EVs) and protein-based nanoparticles have emerged as particularly promising systems.

EVs are nanosized vesicles (30-1000 nm) secreted by all cell types and found in numerous body fluids [7,8]. Their natural composition allows intercellular communication, cargo delivery, and cell-specific recognition via membrane proteins, lipids, and glycans [9-12], making them attractive candidates for tumor-homing strategies [13,14], although the mechanisms governing that EV target specificity remain incompletely understood [15]. Moreover, EVs can evade phagocytosis, circulate longer, and potentially bypass endosomal degradation [16]. Despite these advantages, EVs have limitations, including low drug loading, challenging release kinetics, and sensitivity to environmental factors [17-23]. Furthermore, hydrophilic cargoes encapsulated in EVs often leak during storage, compromising stability [24,25], and current loading methods are not compliant with Good Manufacturing Practice (GMP) standards, limiting clinical translation [26-28].

Silk fibroin nanoparticles (SFNs), on the other hand, offer high drug-loading capacity together with biocompatibility, biodegradability, and tunable release profiles [29-31]. Their surface chemistry, rich in reactive amino acid residues, also enables versatile functionalization for targeted delivery [32-34]. However, unlike EVs, SFNs lack intrinsic biological specificity and cannot replicate the complex surface machinery responsible for cell recognition, making the identification of effective targeting ligands challenging. Many ligands are indeed overexpressed in tumors but still present in healthy tissues, leading to possible off-target interactions [35-38]. Moreover, receptor expression is often heterogeneous across tumor types, within the same tumor, and among patients due to genetic and microenvironmental variability [39-46]. Finally, targeting efficiency is also influenced by ligand density and affinity on the nanoparticle surface, which can affect tissue penetration and selective accumulation [47-50].

This complementarity motivates carrier-in-carrier systems – a hierarchical nanoarchitecture in which a nanoparticle (primary carrier) is associated with the membrane of a biological vesicle (secondary carrier), combining the pharmaceutical properties of the core with the biological functionality of the

vesicular shell. In this design, SFNs provide high drug encapsulation, protection, and controlled release, while EVs confer natural targeting and enhanced cellular uptake. EV-coated SFNs thus represent "smart" drug-delivery systems that align with the principles of precision oncology. This approach is particularly relevant in pleural mesothelioma, an aggressive malignancy with a poor prognosis, median survival below 15 months, and limited treatment options [51-53]. In this context, a drug delivery system capable of efficiently loading cytotoxic drugs, protecting them in circulation, and selectively targeting tumor cells could provide a transformative treatment advance.

Based on these premises, the objective of this study was threefold: (i) to develop a carrier-in-carrier based on SFNs associated with secretome-derived EVs, (ii) to implement a scalable GMP-compliant production method to support future clinical translation, and (iii) to validate the proof-of-concept of EV-coated SFNs as cell-specific nanocarriers. First, the effective formation of a carrier-in-carrier system was preliminarily evaluated by encapsulating SFNs (loaded with curcumin, a lipophilic drug model) within EVs by sonication, and its colloidal stability, protection of the encapsulated active, and drug release were assessed. Subsequently, a GMP-compliant microfluidic encapsulation approach was implemented for the preparation of the carrier-in-carrier systems. Under optimized microfluidic conditions, nanoparticle tracking analysis (NTA) and fluorescence resonance energy transfer (FRET) confirmed the successful formation of EV-coated SFNs. Finally, to assess the biological performance of the developed platform, fluorescent SFNs (made of silk fibroin covalently labeled with fluorescein isothiocyanate, FITC) were membrane-associated with secretome-derived EVs derived from either mesothelioma cells or mesenchymal stromal cells (MSCs) using the microfluidic method, and their uptake was evaluated in tumor versus healthy cell models by tracking fluorescence. Differential internalization confirmed the ability of tumor-derived EVs to favor selective cellular uptake.

2. Materials and methods

2.1 Materials

Silkworm cocoons of *Bombyx mori* were kindly donated by Nembi Industrie Tessili, Capriolo (BS), Italy. Bovine serum albumin (BSA), curcumin, phosphatidylcholine, lithium bromide (LiBr), mannitol, Nile red, sodium carbonate (Na_2CO_3), and sodium bicarbonate ($NaHCO_3$) were purchased from Merck, Milan, Italy. Acetone and dimethyl sulfoxide (DMSO) were purchased from Carlo Erba Reagents, Milan, Italy. Dialysis membranes were purchased from Spectrum Laboratories, Milan, Italy, while easySTRAINER filters were purchased from VWR International, Milan, Italy. MSCs were isolated from adipose tissue according to the procedures reported in [54]. Human fibroblasts were donated by Dr. Marta Cecilia Tosca of the Tissue Bank and Tissue Therapy Unit at Niguarda Hospital, Milan. MISTO mesothelioma cells were donated by Prof. Pinton, Department of

Pharmaceutical Sciences, University of Eastern Piedmont. All reagents and consumables for cell cultures were purchased from Euroclone, Milan, Italy.

2.2 Preparation and characterization of silk fibroin nanoparticles

2.2.1 Extraction and solubilization of silk fibroin

For the extraction of silk fibroin from *Bombyx mori* cocoons, 5 g of cocoons were cut into small pieces (1 × 1 cm), washed under running water, and first degummed by boiling in 2 L of 0.02 M aqueous Na_2CO_3 solution for 30 minutes, with occasional stirring. The fibroin was then washed with distilled water to remove residual salts and sericin, and dried at room temperature. Once completely dry, fibroin was solubilized in aqueous LiBr solution (100% w/v) at 65 °C for 4 hours; the solution was stirred every 30 minutes to improve solubilization (protein conformational transition from Silk II to Silk I). The resulting solution was filtered through an easySTRAINER (70 μm) to remove solid residues, transferred into a dialysis membrane (molecular cut-off: 3.5 kDa), and dialyzed against distilled water for 72 hours at room temperature. The final fibroin concentration was determined gravimetrically after complete water evaporation, and was typically between 6-9% w/v.

2.2.2 Fibroin labeling with FITC

Fibroin in solution was labeled with FITC to allow the preparation of fluorescent SFNs. Briefly, the theoretical number of available lysines was first determined, and fibroin was labeled with FITC at a 1:10 fibroin:FITC molar ratio, to target 10% of the available lysine residues. For the conjugation reaction, fibroin was diluted in carbonate/bicarbonate buffer (0.1 M, pH 9) to a final concentration of 1.67% w/v, then supplemented with FITC stock solution (9.8×10^{-3} M) in DMSO to reach the 1:2 fibroin:FITC molar ratio. The reaction was allowed to proceed overnight at room temperature, protected from light.

2.2.3 Preparation of curcumin-loaded and fluorescent SFNs

To prepare curcumin-loaded SFNs, the aqueous fibroin solution (not labeled with FITC) was diluted to reach a concentration of 1.5% w/v and then added dropwise to acetone, in which curcumin had previously been solubilized at a concentration of 0.08 mg/mL. For the preparation of FITC-SFNs, the aqueous solution of labeled fibroin was diluted with deionized water to a final concentration of 1.5% w/v and then added dropwise to acetone under magnetic stirring, at a fibroin:acetone ratio of 1:5. In both cases, the nanoparticle suspension obtained was dialyzed against distilled water at room temperature for 72 hours using cellulose dialysis tubes with a 3.5 kDa molecular weight cut-off

(MWCO). The suspension was then lyophilized (Christ Epsilon 2-16D LSCplus) at 8×10^{-1} mbar and -50 °C and stored at room temperature until use.

2.2.4 Technological characterization of SFNs

2.2.4.1 Yield, encapsulation efficiency, and drug loading

The percentage yield was calculated according to the equation:

$$Yield\ (\%) = \frac{g\ of\ nanoparticles}{g\ of\ fibroin + g\ of\ active} \times 100$$

The quantification of curcumin in SFNs (drug loading) was assessed by spectrophotometric analysis at 425 nm. Briefly, 1 mg of lyophilized SFNs was dispersed in 10 mL of 96% v/v ethanol and stirred for 72 hours. Subsequently, the SFNs were centrifuged at 4000×*g* for 15 minutes, and the supernatants were collected. The absorbance was then measured using a spectrophotometer (Beckman Coulter, DU 730). The curcumin concentration was determined by extrapolating a calibration curve constructed from the absorbance measurements of curcumin solutions in ethanol (a series of dilutions) over the concentration range of 0.5 µg/mL to 20 µg/mL, with a correlation coefficient (R^2) of 0.998. A 96% v/v ethanol solution was used as the blank. All measurements were performed in triplicate. The amount of loaded curcumin (% w/w) was calculated as the ratio between the total curcumin content (extrapolated from the calibration curve) and the concentration of the analyzed nanoparticles. The encapsulation efficiency (EE%) was determined as the percentage ratio of curcumin effectively entrapped to the curcumin dissolved in acetone during nanoparticle preparation.

2.2.4.2 Particle size analysis

The size distribution of lyophilized SFNs was determined by NTA using a NanoSight NS300 (Malvern Instruments, Malvern, UK) equipped with a 405 nm laser. Nanoparticles were dispersed in ultrapure water at 1 mg/mL and further diluted 1:100 or 1:1000 according to instrument feedback. For each sample, five 60-second measurements were performed; analyses were carried out at 25 °C with a 90° detection angle. Data were processed using NTA 3.0 software and exported to Excel. In addition to size distribution, the average number of nanoparticles per mg of powder was determined; this value was later used for the carrier-in-carrier preparation, as described in Section 2.4.

2.2.4.3 Morphological analysis

The nanoparticles were analyzed morphologically using a Field Emission Scanning Electron Microscope (GeminiSEM-360, Carl Zeiss S.p.A., Milan, Italy). Lyophilized samples were previously

Pt-sputter-coated (thickness: 4 nm) under argon. The samples were imaged at 5 kV, using the InLens SE detector and working distances between around 1.8-2.0 mm.

2.2.4.4 Physicochemical characterization

Infrared spectra were recorded using an Alpha II (Bruker, Rosenheim, Germany) FT-IR spectrometer equipped with an ATR (Attenuated Total Reflection) accessory with a monolithic diamond crystal and a DTGS (Deuterated Triglycine Sulfate) detector. Measurements were performed on multiple samples: SFNs, curcumin, and curcumin-loaded SFNs. ATR FT-IR spectra were measured in the 4000-450 cm^{-1} range, at a resolution of 4 cm^{-1}. Data were processed using Opus 8.7 software. Fluorescence spectra were measured on an FP8500 instrument by Jasco (Jasco Europe, Cremella, Italy) working at a speed of 10000 nm $minutes^{-1}$ and a data interval of 0.5 nm. Suprasil Quartz® cells with an optical path of 1 cm were used.

2.3 Preparation and characterization of secretome-derived *EVs*

2.3.1 Isolation and lyophilization of MSC- and mesothelioma-secretome-derived EVs

The secretome (containing EVs) was isolated from MSCs and MISTO mesothelioma cells as reported in [54]. Adipose-derived MSCs were seeded in flasks (10,000 cells/cm^2) and cultured at 37 °C, 5% CO_2 in DMEM F12 medium supplemented with 10% v/v fetal bovine serum, 1% v/v penicillin/streptomycin, and 1% v/v amphotericin. MISTO mesothelioma cells were cultured in complete RPMI 1640 medium, supplemented with 10% v/v fetal bovine serum, 1% v/v penicillin/streptomycin, and 1% v/v amphotericin. For both cell types, secretome (and thus EV) release was induced by culturing cells in serum-free medium for 48 hours. Conditioned media were collected, centrifuged at 3500× *g* for 10 minutes to remove cell debris and apoptotic bodies, and subsequently ultrafiltered using a tangential flow filtration system (KrosFlo® Research 2i, Spectrum Laboratories, Milan, Italy). A filtration module with a 5 kDa molecular cut-off was used to retain both soluble proteins and EVs. The concentration process was stopped once a standard protein concentration of 115 µg/mL was reached [55]; samples were then diafiltered with sterile deionized water. Mannitol was added to the concentrated and purified secretome to a final concentration of 0.5% w/v; the solution was then lyophilized (Christ Epsilon 2-16D LSCplus) at 8×10^{-1} mbar and -50 °C for 72 hours. The lyophilized product, called lyosecretome, was stored at -20 °C until use (for up to 24 months).

2.3.2 Technological characterization of secretome-derived EVs

In addition to physicochemical properties (see Section 2.2.4.4), the secretome-derived EVs were characterized as reported below.

2.3.2.1 Protein and lipid content

The lyosecretomes obtained were characterized for protein and lipid content using, respectively, the BCA Protein Assay Kit (Thermo Fisher Scientific, Milan, Italy) and the Nile red assay, as reported in [54]. For protein quantification, the absorbance/concentration calibration curve was generated using BSA standards; the reagent was added to each sample and standard at a 1:1 ratio and incubated at 37 °C for 2 hours before measuring absorbance at 562 nm with a microplate reader (Victor Nivo, PerkinElmer, Waltham, MA, USA). Protein concentrations were determined by extrapolating a concentration-absorbance plot of the standards using a third-order polynomial equation ($R^2 = 0.99$). Each sample was tested in triplicate, and results are reported as µg of protein per mg of lyosecretome. For lipid quantification, Nile red powder was dissolved in acetone (3.14 M) and stored at 4 °C, protected from light. The stock solution was diluted 100× in deionized water before use. A volume of 90 µL of lyosecretome dispersed in deionized water at a known concentration was incubated with 10 µL of diluted Nile red solution for 5 minutes, and fluorescence was measured using a microplate reader (Victor, PerkinElmer, Waltham, MA, USA; excitation 530/25 nm, emission 645/40 nm). The fluorescence/concentration calibration curve was generated using phosphatidylcholine standards ($R^2 = 0.99$). Each sample was analyzed in triplicate, and results are reported as µg of lipids per mg of lyosecretome.

2.3.2.2 Particle size analysis

The size distribution of EVs contained in the lyosecretome was analyzed using the method described in Section 2.2.4.2. In this case, the lyophilized sample was resuspended in ultrapure water at 5 mg/mL and diluted 1:100 or 1:1000, as needed, based on instrument feedback. The analysis enabled the determination of both the size distribution and the average number of EVs per milligram of lyosecretome; this value was subsequently used for the carrier-in-carrier preparation, as described in Section 2.4.

2.4 Preparation and characterization of the carrier-in-carrier systems by sonication

2.4.1 Preparation of the carrier-in-carrier systems by sonication

Carrier-in-carrier systems were at first prepared using a sonication-based method. Briefly, lyophilized SFNs were resuspended in deionized water and sonicated (15 minutes) on ice to disrupt aggregates; lyophilized secretome-derived EVs (lyosecretome) were then added at nanoparticle:EV ratios (in

particle number, see Sections 2.2.4.2 and 2.3.2.2) of 1:1, 1:2, and 1:3. For the characterization, the carrier-in-carrier systems were assembled with MSC-secretome-derived EVs, while for the in vitro uptake tests (see Section 2.5) they were also assembled with mesothelioma-secretome-derived EVs. To promote carrier-in-carrier formation, the SFN-EV dispersion was subjected to sonication using an ultrasonic probe equipped with a 0.25" iron tip at 20% amplitude (Q125 sonicator, QSonica L.L.C, Newtown, CT, USA). The procedure consisted of six cycles, each comprising 30 seconds of sonication followed by 30 seconds of rest, repeated for 3 minutes, with a 2-minute cooling period on ice between cycles.

2.4.2 Characterization of the carrier-in-carrier systems

In addition to particle size (see Section 2.2.4.2) and physicochemical properties (see Section 2.2.4.4), the carrier-in-carrier systems were characterized as reported below.

2.4.2.1 Confocal microscopy analysis

A total of 90 µL of the carrier-in-carrier system was taken and incubated with 10 µL of Nile red solution (prepared as described in section 2.3.2.1) for 5 minutes. Samples were placed on a microscope slide and observed using a two-photon confocal microscope (Leica Microsystem, Wetzlar, Germany), using different excitation/emission filters to detect silk (Ex 488 nm; Em 500-550 nm) and the EV lipids labeled with Nile red as described in section 3.3.2 (Ex 543 nm; Em 580-660 nm).

2.4.2.2 Evaluation of curcumin stability

The stability of free curcumin and curcumin encapsulated in different formulations (SFNs and carrier-in-carrier) was evaluated over 8 days in deionized water at room temperature as previously reported [56]. Briefly, free curcumin, curcumin-loaded SFNs, and carrier-in-carrier systems were dispersed in deionized water to achieve a final curcumin concentration of 0.006 mg/mL, and the dispersions were incubated at room temperature in the dark. At predetermined time points (0, 1, 2, 3, 6, and 8 days), the absorbance of each sample was measured at 420 nm using a spectrophotometer (Beckman Coulter, DU 730). Data are reported as the percentage of residual absorbance normalized to the initial value (time 0). All experiments were performed in triplicate.

2.4.2.3. In vitro release test

For each batch, the samples (SFNs and the carrier-in-carriers) were dispersed in deionized water and placed inside a dialysis membrane with a molecular weight cut-off of 3-5 kDa. The membrane was

then immersed in a 50% (v/v) ethanol-water mixture and stirred gently at 37 °C for 3 days. At predetermined time intervals, specific aliquots of the release medium were withdrawn, analyzed using a spectrophotometer (Beckman Coulter, DU 730), and replaced with fresh medium to maintain sink conditions. The curcumin concentration was determined by extrapolating a calibration curve constructed from the absorbance measurements of curcumin solutions in 50% (v/v) ethanol in the concentration range of 0.5 µg/mL to 20 µg/mL, with a correlation coefficient (R^2) of 0.997. The cumulative percentage of drug released was calculated based on the total amount of drug initially encapsulated in SFNs. All formulations (SFNs-CUR, CC1:1, and CC1:2) were tested simultaneously in parallel within the same experimental sessions, under identical conditions and using the same batch of release medium; all measurements were performed in triplicate, and the results are reported as mean values.

2.4.2.4. Drug release kinetic study

The mechanism and kinetics of drug release were characterized by fitting in vitro drug release data to various kinetic models.

Higuchi

$$F(t) = k \times t^{0.5}$$

$$F(t) = 100 \times (1 - C \times \exp^{(-k \times t)})$$

where F(t) is the amount of drug released at time t, and *k* is the release constant. Equation 5 is equation 2.12 from [57].

Peppas-Sahlin

$$F(t) = k_1 \times t^m + k_2 \times t^{(2 \times m)}$$

where F(t) is the amount of drug released at time t, k_1 and k_2 are, respectively, the diffusion and erosion constants, and *m* is the diffusional exponent indicative of the drug release mechanism.

Ritger-Peppas

$$F(t) = k \times t^n$$

where F(t) is the amount of drug released at time t, *k* is the release constant, and *n* is the release exponent, indicative of the drug release mechanism.

Zero-order

$$F(t) = k \times t$$

where F(t) is the amount of drug released at time t, and *k* is the release constant.

Korsmeyer-Peppas

$$F(t) = k_{KP} \times t^n \times Q_0$$

where F(t) is the amount of drug released at time t, k_{KP} is the release constant, n is the release exponent indicative of the drug release mechanism, and Q_0 is the initial amount of drug.

2.5 Development of a microfluidic method for the preparation of the carrier-in-carrier systems

2.5.1 Preparation of the carrier-in-carrier systems by microfluidics

A microfluidic method for the carrier-in-carrier preparation was developed using a GMP-compliant system (Sunshine microfluidic system, Unchained Labs, 4747 Willow Rd, Pleasanton, CA 94588). Batches were prepared by flowing an SFN suspension (1 mg/mL) against an aqueous dispersion of secretome-derived EVs at two different final lipid concentrations (10 or 100 µg/mL) using the Sunny 490 Trident T microfluidic chip (Figure S1). Specifically, the nanoparticle suspension was introduced into the channel marked by the green arrow to be "wrapped" by the secretome-derived EVs introduced in the channel marked by the red arrow. The instrument allows setting the total flow rate (the sum of SFN and EV flows) and the flow ratio, expressed as both volumetric and flow ratios. In this study, the total flow rate was modulated while maintaining the EV flow rate at or near the maximum allowed (10,000 µL/min), and the SFN flow rate was varied according to the ratios reported in Table 1. The total flow rate uniquely identifies each experimental condition, since each value corresponds to a specific volumetric and flow ratio between SFNs and secretome-derived EVs.

Table 1. Flow conditions used for the preparation of the carrier-in-carriers with microfluidics.

Total flow rate (µL/min)	**Ratio**		**Nanoparticle flow rate (µL/min)**	**EV flow rate (µL/min)**
	SFNs	**EVs**		
20,000	1	1	10,000	10,000
15,000		2	5000	10,000
13,000		3	3250	9750
12,500		4	2500	10,000
12,000		5	2000	10,000
11,000		10	1000	10,000

Overall, five experimental groups were prepared (Table 2): two carrier-in-carrier formulations containing SFNs (1 mg/mL) embedded in secretome-derived EVs at 10 or 100 µg/mL (CC10 and CC100); as controls, secretome-derived EVs were fluxed alone at 10 or 100 µg/mL (EVs 10 and EVs 100), and SFNs at 1 mg/mL. All samples were prepared or processed under the flow conditions described in Table 1. For each condition, three batches were prepared.

Table 2. Experimental groups and their compositional characteristics.

Group	SFNs	EVs	SFN concentration	EV concentration	Description
CC10	Yes	Yes	1 mg/mL	10 μg/mL	Carrier-in-carrier with SFNs and secretome-derived EVs at 10 or 100 μg/mL
CC100				100 μg/mL	
EVs 10	No	Yes	0	10 μg/mL	Secretome-derived EV-only control (10 or 100 μg/mL), no NP
EVs 100				100 μg/mL	
SFNs	Yes	No	1 mg/mL	0	SFN-only control (1 mg/mL), no secretome-derived EV

2.5.2 Evaluation of effective carrier-in-carrier formation

The effective formation of carrier-in-carrier systems via microfluidics was confirmed by analyzing particle size for each experimental group (Table 2), prepared under the flow conditions indicated in Table 1, and by FRET analysis, as detailed below. Each analysis was conducted on three different batches.

2.5.2.1 Particle size analysis

The size distribution of carrier-in-carrier systems was analyzed as described in Section 2.2.4.1. In this case, each diluted sample was analyzed either as it is (non-sonicated) or after 5 minutes of sonication using an ultrasonic probe with a 0.25" iron tip at 20% amplitude (Q125 sonicator, QSonica L.L.C, Newtown, CT, USA).

2.5.2.2 Fluorescence Resonance Energy Transfer (FRET)

The experiment was carried out using FRET between SFNs prepared with FITC-labeled fibroin (donor, see Section 2.2.3) and Nile red-labeled EVs (acceptor, see Section 2.3.2.1). Fluorescence was recorded upon excitation at 478 nm (λ_{exc} FITC), monitoring emission at 515 nm (FITC) and 620 nm (Nile red). Samples were prepared under the flow conditions listed in Table 1 and analyzed as summarized in Figure S2. Besides FRET-responsive carrier-in-carrier systems (FITC-SFNs and Nile red-labeled EVs), the following control samples were measured under the same conditions: (i) secretome-derived EVs alone and carrier-in-carrier systems with non-fluorescent SFNs, with or

without Nile red labeling, to establish baseline fluorescence and confirm that direct excitation of Nile red at 478 nm was negligible; (ii) FITC-SFNs physically mixed with unlabeled secretome-derived EVs (not assembled into carrier-in-carrier systems) to exclude EV-induced quenching of FITC fluorescence independent of FRET, such as inner filter effects or collisional quenching; and (iii) FITC-SFNs physically mixed with Nile red-labeled secretome-derived EVs (not assembled into carrier-in-carrier systems) to exclude FRET unrelated to carrier-in-carrier architecture. For FRET-responsive samples, FRET efficiency (E) was calculated as follows:

$$E = \left(1 - \frac{F_{DA}}{F_D}\right) \times 100$$

where F_D represents the donor fluorescence intensity in the absence of acceptor, and F_{DA} the donor fluorescence intensity in the presence of acceptor. FRET efficiency values were also used as a semi-quantitative proxy for coating completeness, as described in the Results and Discussion section.

2.6 Cellular uptake assay to evaluate cell-specific targeting of the carrier-in-carrier systems

The cellular uptake of carrier-in-carrier systems produced by the microfluidic method was evaluated in healthy (MSC and fibroblasts) and tumor (MISTO mesothelioma) cell lines. In particular, uptake studies were performed on selected microfluidic formulations corresponding to SFN/EV ratios of 1:1, 1:2, and 1:3, prepared at total flow rates of 20,000, 15,000, and 13,000 μL/min, respectively, using secretome-derived EVs at 100 μg/mL. These conditions were chosen based on FRET analysis, which demonstrated efficient carrier-in-carrier formation under these parameters. Both MSC-derived EVs and mesothelioma-derived EVs were employed to generate the corresponding carrier-in-carrier systems. In each well of a 96-well plate, 250 μL of cell suspension containing 7500 cells were seeded, using cell-specific complete culture media (for MSCs and mesothelioma cells, see Section 2.3.1; for fibroblasts: DMEM HG supplemented with 10% v/v fetal bovine serum, 1% v/v penicillin/streptomycin, and 1% v/v amphotericin). Cells were incubated at 37 °C and 5% CO_2 for 4 days; thereafter, the culture medium was replaced with serum-free, phenol-red-free medium containing SFNs or carrier-in-carrier systems. Samples were dispersed at final SFN component concentrations of 0.2 and 0.4 mg/mL and incubated for 30, 60, and 120 minutes. At the end of incubation, the media were removed, cells were washed three times with PBS, and cellular fluorescence (FITC-labeled fibroin) was measured with a plate reader (Victor Nivo, PerkinElmer, Waltham, MA, USA; excitation at 480 nm, emission at 530 nm). Untreated cells were used as controls.

2.7 Statistical analysis

Raw data were processed using STATGRAPHICS XVII (Statpoint Technologies, Inc., Warrenton, Virginia, USA) or GraphPad Prism (version 10.0.0, GraphPad Software, Boston, MA, USA). Statistical analysis was performed using multifactorial analysis of variance (ANOVA) followed by the Least Significant Difference (LSD) post hoc test for multiple comparisons. Differences were considered statistically significant at $p < 0.05$.

3. Results and discussion

In recent years, the need to develop and produce drug delivery systems that combine transport and selective targeting has become increasingly evident, aiming to minimize side effects while enhancing therapeutic efficacy. This challenge is particularly relevant in the framework of precision oncology, where treatments are designed to selectively act on tumor cells while sparing healthy tissues. In this context, this work focused on a carrier-in-carrier system in which SFNs are coated with the EV fraction of a GMP-compliant lyosecretome, aiming to combine the strengths of both nanoparticles while overcoming their limitations – for instance, by increasing drug efficacy, reducing off-target effects, and enabling advanced tumor-homing strategies for cancer therapy. Specifically, secretome-derived EVs enable biological recognition and intrinsic targeting, whereas SFNs provide higher drug-loading capacity and greater physicochemical stability.

Based on these premises, the objective of this study was threefold: (i) to develop a carrier-in-carrier systems by based on SFNs coated with secretome-derived EVs via sonication and to preliminarily assess their formation, colloidal stability, protection of the encapsulated active, and drug release; (ii) to implement a scalable, GMP-compliant microfluidic encapsulation method for the preparation of the carrier-in-carrier system and to confirm its successful formation; and (iii) to validate the proof-of-concept of EV-coated SFNs as cell-specific nanocarriers by evaluating the uptake of fluorescently labeled SFNs encapsulated in mesothelioma- or MSC-secretome-derived EVs produced via the microfluidic approach, in tumor versus healthy cell models.

To address the first objective, SFNs were prepared by fibroin desolvation in acetone, in which curcumin had been previously solubilized. The process yield was 78.6%, with a curcumin loading of 6.23 ± 0.91% (w/w) and an encapsulation efficiency of 43.3 ± 7.8%. SEM analysis revealed round-shaped particles with a tendency to form clusters (Figure S3). EVs were obtained from MSCs and MISTO mesothelioma cells as part of a lyosecretome preparation, defined as a freeze-dried formulation of the full conditioned medium processed by tangential flow filtration and lyophilization in the presence of mannitol. This approach is deliberately designed to retain EVs within their native secreted environment, avoiding ultracentrifugation or density gradient steps that compromise vesicle integrity and are incompatible with GMP-scale production [54,55,58]. Evidence for the identity of the

EV component within both preparations is supported by data from previous publications of our group: CD63 and RAB27b expression (Western blot) and NTA size profiling consistent with the small EV range (mean diameter ~145 nm) have been reported for mesothelioma-derived preparations using the same MISTO cell line and isolation protocol [58], in agreement with the size distributions measured in the present study and reported below. Similarly, MSC-derived lyosecretome has been shown to be enriched in EV-associated proteins by quantitative proteomic analysis [54]. The resulting lyosecretomes exhibited a protein content of 22.4 ± 0.07 μg/mg and a lipid content of 9.69 ± 0.54 μg/mg powder if derived from MSCs, and a protein content of 23.7 ± 0.23 μg/mg and a lipid content of 8.03 ± 2.66 μg/mg powder if derived from mesothelioma cells.

SFNs and secretome-derived EVs were combined in a carrier-in-carrier structure through sonication, a method shown to achieve efficient encapsulation without significantly altering the EV composition [8,59] (Figure 1A). Specifically, during sonication, ultrasound disrupts EVs through cavitation; upon cessation of ultrasound, the phospholipid components rearrange into vesicles that assemble around SFNs, acting as nucleation centers [59]. Different SFN-to-EV ratios were tested (1:1, 1:2, and 1:3). To verify the actual formation of the carrier-in-carrier system, confocal microscopy analysis was performed. For all SFN/EV ratios tested, an overlap of fibroin and Nile red fluorescence was observed, indicating co-localization of SFNs and secretome-derived EVs (Figure S4). To elucidate the spatial organization of SFNs and secretome-derived EVs relative to one another, regions exhibiting fluorescence overlap were analyzed along the Z-plane. Assuming a spherical geometry consistent with SFN morphology, the fluorescence pattern showed a recurrent distribution, with red fluorescence (EVs) predominating at the lower and upper regions of the system, while green fluorescence (SFNs) was more prominent in the central region, surrounded by red signal (Figure 1B, supplementary Video S1). This distribution across the Z-stack is consistent with the spatial association of SFNs and secretome-derived EVs within the carrier-in-carrier system, although it should be noted that – given the particles fall below the lateral resolution limit of conventional confocal microscopy – these patterns reflect ensemble co-localization within diffraction-limited volumes rather than direct visualization of discrete carrier-in-carrier architecture consistent with membrane association.

For SFNs, NTA measurements confirmed a mean hydrodynamic diameter of 183.6 ± 5.3 nm, with a size distribution spanning from 130 nm (d_{10}) to ~255 nm (d_{90}) (Figure 1C), consistent with previous reports [60-62]. For secretome-derived EVs from both MSCs and mesothelioma cells, the size distribution analysis showed a mean hydrodynamic diameter of 182.8 ± 4.9 nm and 162.2 ± 4.9 nm, respectively. This is consistent with the typical size range of small EVs, with a broad distribution extending up to 250 nm (Figure 1C). NTA measurements confirmed changes in particle size and

distribution following the formation of the carrier-in-carrier system, resulting in a more homogeneous, dispersed system with a smaller average particle size than in the single-carrier formulation, likely due to partial disaggregation of SFN clusters during assembly.

The samples were also characterized for their physico-chemical properties (Figure 1D). For SFNs, ATR-FTIR analysis showed that fibroin, the main constituent of SFNs and the carrier-in-carrier system, exists in its stable conformation (crystalline conformation, Silk II), characterized by a high content of β-sheets. Indeed, FTIR analyses allowed the identification of β-sheets in the spectral region of Amide I (around 1620 cm^{-1}, ν_{CO}), Amide II (around 1520 cm^{-1}, $\delta_{NH} + \nu_{CN}$), and Amide III (around 1230 cm^{-1}, $\nu_{CN} + \delta_{NH}$). An amide A signal is present in the high-frequency region at 3277 cm^{-1} (νNH) (Figure 1D, black line). The typical absorption bands of curcumin appear at 1626 cm^{-1} ($\nu_{CO} + \nu_{CC}$) and 1505 cm^{-1}, associated with the stretching vibration of conjugated C=O. Furthermore, signals at 1272 cm^{-1} and 1150 cm^{-1} are attributed to the stretching vibrations of the Csp3-O and Csp2-O bonds, respectively. Ring stretching modes give rise to bands at 1603 cm^{-1} as well as in the 1460-1410 cm^{-1} region. At high frequencies, the signal at 3506 cm^{-1} is associated with the stretching mode of H-bonded OH groups. (Figure 1D, red line). Although the IR spectrum of SFNs loaded with curcumin (Figure 1D, green line) is dominated by the characteristic bands of fibroin (Amide I, Amide II and Amide III bands), the contribution of curcumin absorption bands can be mainly identified by the increase in the relative intensity of Amide II band with respect Amide I band, thanks to the contribution of the C=O stretching band expected at 1505 cm^{-1}. At lower frequencies, weak signals in the 1200-900 cm^{-1} range, indicated with an asterisk, are associated with curcumin too. In the FITR spectrum of secretome-derived EVs (Figure S5), the identification of typical absorption of secretome constituents is not straightforward due to the intense contributions of the cryoprotectant's vibrational bands. It has to be considered that the percentage of cryoprotectant (mannitol) reaches 99%, while only 1% consists of EV's typical phospholipids. As a consequence, typical signals from EVs cannot be unambiguously identified. Nevertheless, the presence of the components of the secretome-derived EVs is testified by the modifications of the mannitol spectrum in the vCH region (3000-2800 cm^{-1}), in the 1500-1300 cm^{-1} region, where deformations of CH_2 and CH_3 groups can be found, and in the lower frequencies region, where fundamental vibrations of phospholipids are usually present. In the carrier-in-carrier samples (figure 1 D, blue curve), beside expected contributions form fibroin (Amide A, Amide I, Amide II and Amide III bands), signals clearly associated with secretome-derived EVs arise, such as bands at 1743 cm-1 ($\nu_{C=O}$ in esters), 1454 cm^{-1} and complex set of bands in the 1400-1300 cm^{-1} range (δ_{CH_2/CH_3}) along with increased intensity of CH_2 and CH_3 stretching signals (2950-2900 cm^{-1}). No significant differences were observed between the IR spectra of carrier-in-carrier batches prepared with different SFN/EV ratios (Figure S6).

The colloidal stability of the carrier-in-carrier system was investigated by measuring particle size over time and comparing it with that of SFNs and secretome-derived EVs alone (Figure 1E). The mean diameter of SFNs showed a marked variation over time, with an initial decrease during the first three days, followed by a sharp increase at day 15 (likely indicative of aggregation) and a subsequent reduction. Secretome-derived EVs displayed stable diameters up to day 20, followed by a moderate increase, possibly due to lipid bilayer fusion or aggregation. In contrast, the carrier-in-carrier systems maintained a consistent mean diameter (165-180 nm) throughout the study, indicating a stabilizing effect of the secretome-derived EV coating. Similar temporal trends were observed for the mode, d_{10}, and d_{50} parameters: SFNs underwent alternating aggregation and disaggregation phases, while secretome-derived EVs remained stable until day 20; in all the carrier-in-carrier systems, these parameters remained statistically unchanged over time and across different SFN/EV ratios. The analysis of d_{90} values showed instead that secretome-derived EVs reached up to 300 nm, the carrier-in-carrier systems occupied an intermediate range (~230 nm), and SFNs remained between 200 and 250 nm. Importantly, the stability characteristics of the carrier-in-carrier system were not significantly dependent on the SFN/EV ratio, as even the 1:1 ratio yielded a homogeneous, stable structure over time. Overall, the stability of the carrier-in-carrier particle size over time – showing no aggregation or disaggregation phenomena compared to secretome-derived EVs and SFNs alone – indicates the homogeneity of the nanoparticle coating process with EVs and corroborates the findings from confocal analysis: since all SFNs were coated with secretome-derived EVs following carrier-in-carrier formation, the resulting population was less prone to aggregation or disassembly. This behavior can likely be attributed to the mechanical barrier provided by the EV lipid layer, which prevented particle-particle adhesion.

The protective capacity of the formulated carrier-in-carrier system against curcumin degradation was evaluated by monitoring over time the residual absorbance of curcumin – either free, encapsulated in SFNs, or incorporated in the carrier-in-carrier systems. Figure 1F shows the percentage of residual absorbance normalized to the initial value at time 0 (100%). Free, unencapsulated curcumin exhibited significant degradation within the first day, dropping to 40% residual absorbance and further declining to 20% by day 8. This is consistent with previous findings reporting curcumin instability in water, which leads to rapid hydrolysis and subsequent molecular fragmentation [63]; more specifically, Wang et al. reported that 90% of curcumin degraded within 30 minutes in phosphate buffer at pH 7.4, forming products such as trans-6-(4'-hydroxy-3'-methoxyphenyl)-2,4-dioxo-5-hexenal, ferulic aldehyde, ferulic acid, feruloylmethane, and vanillin [64]. Encapsulation improved the curcumin stability: SFNs loaded with curcumin retained 50% of absorbance on day 1, with the absorbance remaining constant thereafter. The carrier-in-carrier formulations provided even greater

protection: following an initial 40-45% loss on day 1, residual curcumin stabilized at 55-60% over time, with no significant changes at later points. Notably, the SFN/EV 1:1 formulation offered superior protection during the first three days; by days 6 and 8, protection levels of both carrier-in-carrier formulations were comparable. Overall, these results suggest that the developed carrier-in-carrier system effectively shields curcumin from hydrolytic degradation, enhancing its potential for therapeutic application.

The release profile of curcumin (Figure 1G) revealed that coating SFNs with secretome-derived EVs markedly slowed down the drug release, indicating that the EV membrane is an additional diffusion barrier. Fitting of the release data to kinetic models (Table 3) showed that release from both SFNs and carrier-in-carrier systems involves contributions of both diffusion and case-II relaxation mechanisms. The Peppas-Sahlin model indicates that the relaxation-controlled term (k_2) is the dominant contribution across all formulations, while the diffusive term (k_1) is negative and of smaller absolute magnitude – a feature that reflects the opposing contribution of the diffusive term in the early release phase within β-sheet-rich silk fibroin matrices [57], and is statistically robust as confirmed by the 95% confidence bounds reported in Table 3. Independently, the Ritger-Peppas model yields release exponents *n* of 0.40-0.47 across all formulations, indicative of anomalous (non-Fickian) transport consistent with the coexistence of diffusion and relaxation mechanisms. The difference between the *m* coefficient from the Peppas-Sahlin model and the *n* exponent from the Ritger-Peppas equation further supports this interpretation. Overall, the slower release observed in the carrier-in-carrier systems is primarily attributable to the EV membrane decreasing the diffusion rate of curcumin, while the internal SFN matrix retains its intrinsic relaxation-controlled contribution. Importantly, comparison of the cumulative release plateaus indicates that the total releasable fraction of curcumin is preserved upon secretome-derived EV coating, suggesting no significant drug loss during the sonication-based assembly process.

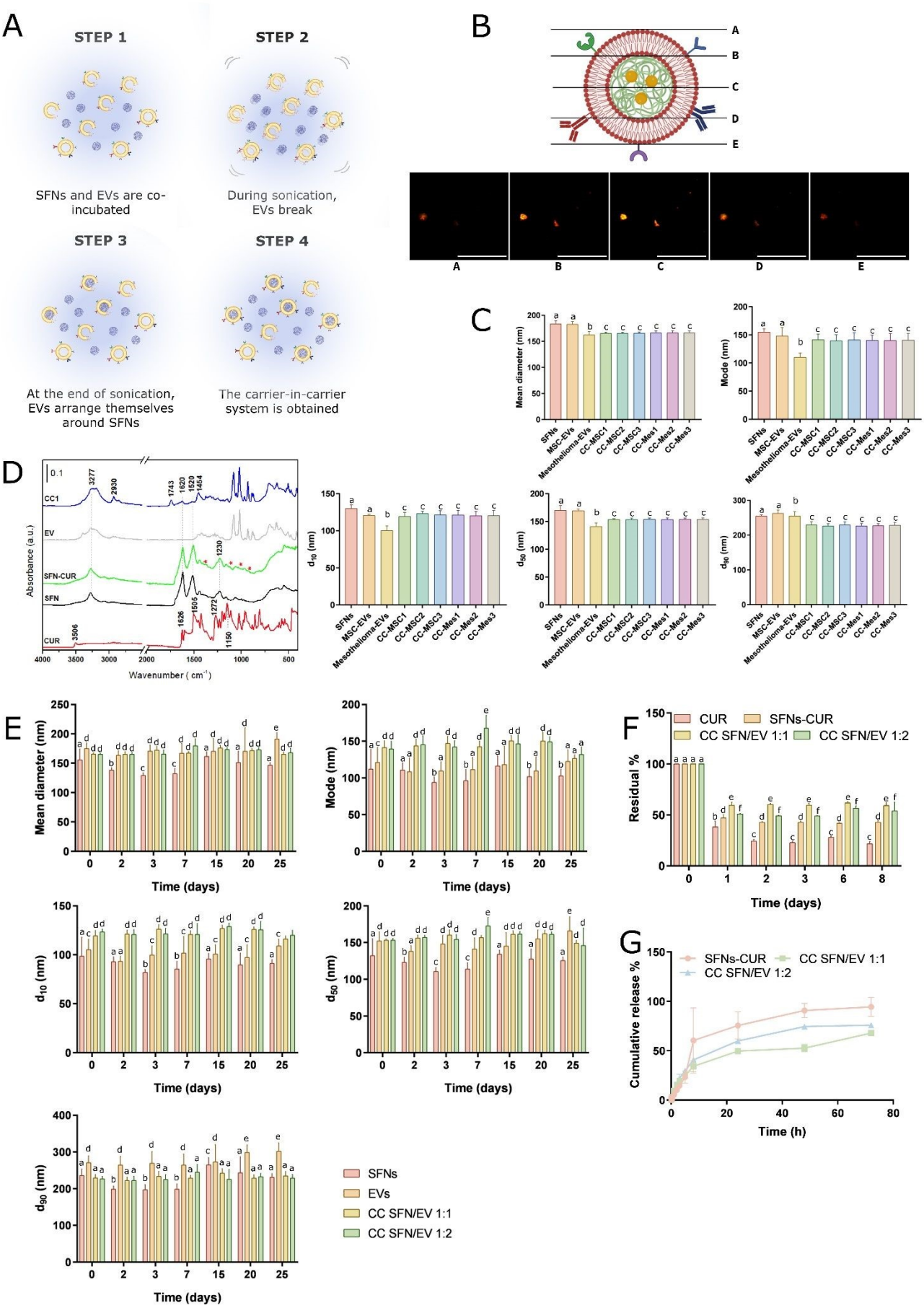

Figure 1. Preparation and characterization of the carrier-in-carrier by sonication. (**A**) Schematic illustration of the formation of the carrier-in-carrier system by sonication. (**B**) Confocal fluorescence analysis (Z-stack) of the carrier-in-carrier system: SFNs are green, and secretome-derived EVs are red (marked with Nile red). Scale bar: 10 μm. The image reflects ensemble co-localization of SFN and secretome-derived EV fluorescence within the detection volume rather than a resolved single-particle core-shell architecture. (**C**) Particle size of carrier-in-carrier samples prepared via sonication. Data are reported as mean values ± standard deviation; Multifactor ANOVA followed by LSD post-hoc, n = 5. Different letters indicate a significant difference ($p < 0.05$), whereas the same letter indicates a non-significant difference ($p > 0.05$). (**D**) ATR-FTIR spectra of SFNs (black line), curcumin (red line), curcumin-loaded SFNs (green line), secretome-derived EVs (gray line), and the carrier-in-carriers prepared with a 1:1 SFN/EV ratio (blue curve). (**E**) Colloidal stability of SFNs, secretome-derived EVs, and the carrier-in-carrier systems in PBS at 4 °C. Data are reported as mean values ± standard deviation; Multifactor ANOVA followed by LSD post-hoc, n = 5. Different letters indicate a significant difference ($p < 0.05$), whereas the same letter indicates a non-significant difference ($p > 0.05$). (**F**) Residual curcumin absorbance % across different formulations (curcumin in solution, CUR; curcumin encapsulated in SFNs, SFNs-CUR; and curcumin encapsulated in the carrier-in-carrier system prepared with SFN/EV ratios of 1:1, CC1:1, and 1:2, CC1:2) as a function of time. Data are reported as mean value ± standard deviation; Multifactor ANOVA followed by LSD post-hoc, n = 3. Different letters indicate a significant difference ($p < 0.05$), whereas the same letter indicates a non-significant difference ($p > 0.05$). (**G**) Cumulative release % of curcumin from nanoparticles (SFNs-CUR) and from the carrier-in-carrier system prepared with SFN/EV ratios of 1:1, CC1:1, and 1:2, CC1:2. Data are reported as mean values ± standard deviation, Multifactor ANOVA followed by LSD post-hoc, n = 3.

Table 3. Results of in vitro release model fitting for curcumin release from samples. Kinetic elaborations were performed on the cumulative release data obtained from at least three independent experiments for each batch.

Model	Equation	Sample	Coefficients (95% Confidence Bounds)	Sum of Squares	R^2	Degrees of Freedom
Higuchi	$F(t) = k \times t^{0.5}$	SFNs-CUR	k = 0.1141 (0.1001, 0.1281)	0.3096	0.8729	21
		CC1	k = 0.02318	0.004738	0.9395	21

			(0.02145, 0.02490)			
		CC2	k = 0.02819 (0.02609, 0.03029)	0.006998	0.9422	21
	$F(t) = 100 \times (1 - C \times \exp^{(-k \times t)})$	SFNs-CUR	C = 0.9988 (0.9978, 0.9997) k = 0.0001262 (9.31×10^{-5}, 1.610×10^{-4})	0.6298	0.7414	22
		CC1	C = 0.9997 (0.9995, 0.9998) k = 0..00002348 (1.811×10^{-5}, 2.886×10^{-5})	0.01518	0.8062	22
		CC2	C = 0.9996 (0.9994, 0.9998) k = 0.00002892 (2.197×10^{-5}, 3.588×10^{-5})	0.02539	0.7904	22
Peppas-Sahlin	$F(t) = k_1 \times t^m + k_2 \times t^{(2 \times m)}$	SFNs-CUR	k_1 = -0.6428 (-3.144, 0.02945) k_2 = 0.7357 (0.001771, 3.247) m = 0.1155 (0.04033, 0.2542)	0.2526	0.8963	22
		CC1	k_1 = -0.1543 (-0.3333, -0.05877) k_2 = 0.1837 (0.08927, 0.3633) m = 0.09326 (0.05893, 0.1372)	0.001416	0.9819	22

		CC2	k_1 = -0.2009 (-0.4018, -0.08935) k_2 = 0.2334 (0.1232, 0.4349) m = 0.09315 (0.06126, 0.1323)	0.0021	0.9827	22
Ritger-Peppas	$F(t) = k \times t^n$	SFNs-CUR	k = 0.1295 (0.07846, 0.1891) n = 0.4654 (0.3612, 0.5946)	0.304	0.8752	22
		CC1	k = 0.003349 (0.02781, 0.03944) n = 0.3984 (0.3528, 0.4485)	0.002622	0.9665	22
		CC2	k = 0.0389 (0.03167, 0.04656) n = 0.4113 (0.3616, 0.4663)	0.004575	0.9622	22
Zero-order	$F(t) = k \times t$	SFNs-CUR	k = 0.01504 (0.01172, 0.01835)	0.8727	0.6416	22
		CC1	k = 0.003011 (0.002373, 0.003648)	0.03227	0.5881	22
		CC2	k = 0.003658 (0.002878, 0.004438)	0.0483	0.6012	22
Korsmeyer-Peppas	$F(t) = k_{KP} \times t^n \times Q_0$	SFNs-CUR	k_{KP} = 0.1295 (0.07846, 0.1891) n = 0.4654	0.304	0.8752	22

			(0.3612, 0.5946)			
		CC1	k_{KP} = 0.03349 (0.02781, 0.03944) n = 0.3984 (0.3528, 0.4485)	0.002622	0.9665	22
		CC2	k_{KP} = 0.0389 (0.03167, 0.04656) n = 0.4113 (0.3616, 0.4663)	0.004575	0.9622	22

The sonication experiments described above served as an exploratory proof-of-concept phase, establishing that carrier-in-carrier formation is achievable, that secretome-derived EV coating confers colloidal stability and curcumin protection, and that the assembled system produces a sustained, diffusion-controlled release profile. Having validated the concept at this preliminary stage, the production method was subsequently translated to a GMP-compliant microfluidic approach (Figure 2A). The two methods are therefore not parallel alternatives but sequential stages in the development of the platform: sonication for concept validation, microfluidics for translatable production. Compared to sonication, the microfluidic approach offers full and continuous control over process parameters (flow rate, volumetric ratio), intrinsic scalability through continuous flow processing, and compatibility with pharmaceutical manufacturing standards. Additionally, the lower mechanical stress associated with microfluidic processing is expected to be compatible with improved preservation of drug content during assembly compared to probe sonication.

In the microfluidic setup, SFNs and secretome-derived EVs were co-flowed at defined ratios and flow rates within the microfluidic chip. Unlike the sonication method, in which the SFN-to-EV ratio was defined by particle number, the microfluidic process was based on mass, quantifying secretome-derived EVs as μg of lipid. This enabled precise and reproducible control of formulation parameters in accordance with pharmaceutical manufacturing standards. The concentration of SFNs was maintained at 1 mg/mL, while EV lipid concentrations of 10 and 100 μg/mL were tested to identify the optimal condition for complete nanoparticle surface coating. Experiments were conducted under different flow regimes (μL/min) to evaluate the effect of hydrodynamic conditions on carrier-in-carrier formation. In detail, the total flow rate was adjusted while maintaining the EV flow near the

upper operational limit (10,000 μL/min), and the nanoparticle flow was proportionally reduced to achieve the desired ratios. Carrier-in-carrier formation was verified by NTA and FRET assays.

The NTA analysis (Figure 2B) assessed particle size distributions to determine whether the carrier-in-carrier systems exhibited distinct particle sizes compared to their single components (SFNs or secretome-derived EVs). The statistical analysis confirmed a significant effect of both the sample ($p<0.001$) and the flow rate ($p<0.001$). For each sample, the trends of mean diameter, mode, d_{10}, and d_{50} as a function of flow rate were consistent. SFNs showed a significant increase in size when processed at flow rates of 13,000 μL/min or higher, suggesting aggregation. For instance, the mean diameter of SFNs processed at 11,000, 12,000, and 12,500 μL/min did not differ significantly, whereas it was significantly smaller compared to SFNs processed at 13,000, 15,000, and 20,000 μL/min. The only exception was d_{90}, which did not vary significantly with flow rate. A similar trend was observed for the carrier-in-carrier systems: both the carrier-in-carrier prepared with secretome-derived EVs at 10 and 100 μg/mL showed significant increases in d_{10}, d_{50}, mean, and mode as the total flow increased, while d_{90} values remained unchanged. For example, in the batches prepared with secretome-derived EVs at 10 μg/mL, the values of d_{10}, d_{50}, mean, and mode at 11,000, 12,000, and 12,500 μL/min were significantly lower compared to those at 15,000 and 20,000 μL/min. For the carrier-in-carrier systems prepared with secretome-derived EVs at 100 μg/mL, this difference was sometimes less pronounced and in some cases non-significant; for instance, no significant difference was observed between d_{90} at 13,000 μL/min and 15,000 μL/min. Overall, increasing the EV lipid concentration (from 10 to 100 μg/mL) altered the size of the carrier-in-carrier systems: the system prepared with secretome-derived EVs at 10 μg/mL showed a particle size trend resembling that of SFNs, while the one prepared with secretome-derived EVs at 100 μg/mL displayed values closer, though still significantly different, to those of EVs alone. Samples consisting solely of secretome-derived EVs showed either stable or significantly reduced particle size with increasing flow. Collectively, the particle size profiles of the carrier-in-carrier systems differed from those of SFNs or secretome-derived EVs alone, particularly at 13,000, 15,000, and 20,000 μL/min, suggesting a different component organization compatible with the formation of carrier-in-carrier architectures. Across all samples, d_{90}-d_{10}, which is indicative of the width of the particle size distribution (higher values equal greater heterogeneity in dimensions), did not vary significantly with flow rate, except for secretome-derived EVs at 100 μg/mL and 13,000 μL/min, which showed marked heterogeneity.

The effect of sonication on particle size was then assessed to gain insights into stability (Figure 2C). Sonication had a generally significant impact on particle size ($p<0.001$). Specifically, for secretome-derived EVs and the carrier-in-carrier systems prepared with secretome-derived EVs at 100 μg/mL, the sonication led to a significant increase in mean diameter, mode, median, and all percentile

diameters. In contrast, in SFNs and in carrier-in-carrier systems preparations with secretome-derived EVs at 10 μg/mL, sonication either had no effect or, when significant, reduced particle size. For example, in these two systems, sonication decreased mean, mode, and d_{50}, and significantly reduced d_{90} in batches prepared with secretome-derived EVs at 10 μg/mL, while d_{10} remained largely unaffected. With respect to d_{90}-d_{10}, sonication was generally non-significant, except for the carrier-in-carrier systems prepared with secretome-derived EVs at 10 μg/mL, where particle populations became more homogeneous.

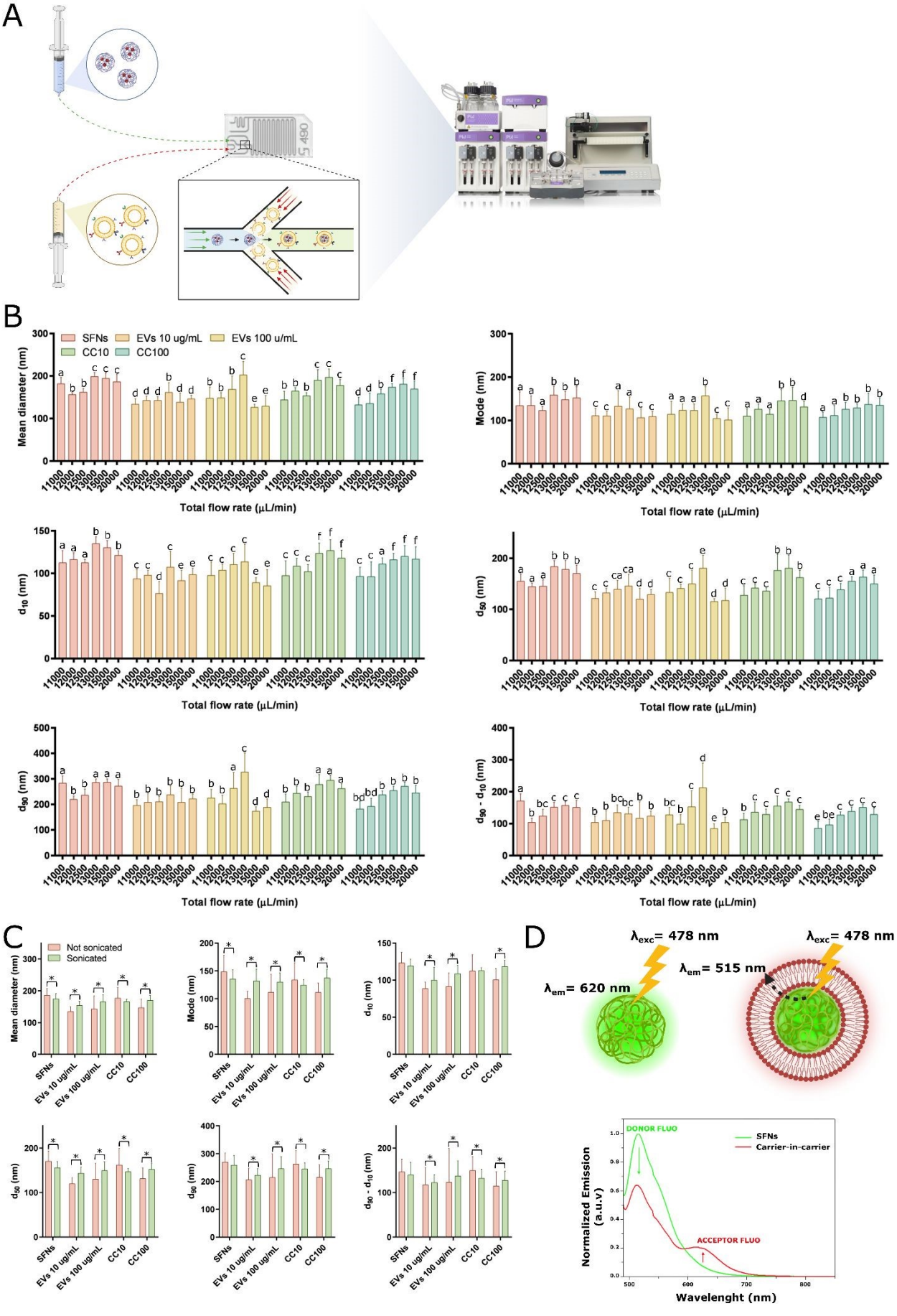

Figure 2. Preparation and characterization of the carrier-in-carrier systems by microfluidics. **(A)** Schematic illustration of the formation of the carrier-in-carrier by microfluidics. (**B**) Particle size of the carrier-in-carriers samples prepared via microfluidics, or of SFNs and secretome-derived EVs processed with the same flow conditions used for the preparation of the carrier-in-carriers. The mean diameter, mode, d_{10}, d_{50}, d_{90}, and d_{90}-d_{10} are reported for each group as a function of total flow rate. Data are reported as mean value ± LSD; Multifactor ANOVA followed by LSD post-hoc, n=3. Different letters indicate significant differences ($p<0.05$), while the same letter indicates non-significant differences ($p>0.05$). (**C**) Effect of sonication on particle size of samples prepared by microfluidics. The mean diameter, mode, d_{10}, d_{50}, d_{90}, and d_{90}-d_{10} are reported for each group as a function of total flow rate. * indicate significant differences ($p<0.05$). Data are reported as mean value ± LSD; Multifactor ANOVA followed by LSD post-hoc, n=3. (**D**) Emission spectra of fluorescent SFNs alone (green line) or of carrier-in-carrier containing fluorescent SFNs with Nile red labeling (red line).

FRET analyses provided further confirmation of the spatial organization of components and correct carrier-in-carrier assembly. Control samples (secretome-derived EV only or carrier-in-carrier with non-fluorescent SFNs) excited at 478 nm showed no significant emission at 620 nm, as expected (Figure S7, green line). Nile red addition produced only weak fluorescence (peak intensities of 5 CPS for EV and 7 CPS for non-fluorescent carrier-in-carrier), confirming negligible direct excitation of Nile red at 478 nm (red line). As a further control to exclude any possible FRET in the absence of carrier-in-carrier architectures, FITC-SFNs were physically mixed with Nile red-labeled secretome-derived EVs without microfluidic assembly; this condition showed no significant emission above the baseline established by the EV-only controls (Figure S8), demonstrating that the mere physical co-presence of donor- and acceptor-labeled components in dispersion – without the spatial proximity achieved through microfluidic assembly – is insufficient to generate a FRET signal. Together, these controls confirmed that, in the absence of specific donor-acceptor interactions, no acceptor fluorescence was detected upon donor excitation, excluding potential artifacts from direct acceptor excitation, inner filter effects, or non-specific quenching. In contrast, carrier-in-carriers containing FITC-SFNs enabled Nile red excitation through FRET, yielding markedly higher emission intensities (~500 CPS) (Figure 2D), confirming efficient energy transfer and therefore nanoscale proximity between SFNs and secretome-derived EV membranes. FRET efficiency (E%) was then calculated for all carrier-in-carriers prepared with fluorescent nanoparticles and secretome-derived EV (10 or 100 μg/mL), under the flow conditions reported in Table 1; results are summarized in Table 4.

Table 4. FRET efficiency of carrier-in-carriers prepared with FITC-SFNs and secretome-derived EVs (10 or 100 μg/mL), under specific flow conditions. F_{DA}: donor fluorescence in the presence of acceptor; F_D: donor fluorescence without acceptor.

Total flow rate (μL/min)	Ratio		EV concentration (μg/mL)	F_D	F_{DA}	E%
	SFNs	EVs				
20,000	1	1	10	2467.59	1577.13	36.09
15,000		2		5251.77	3781.54	27.99
13,000		3		3388.52	2509.49	25.94
12,500		4		380.76	395.62	-3.90
12,000		5		303.87	337.59	-11.1
11,000		10		0	0	0
20,000	1	1	100	2414.34	1467.95	39.20
15,000		2		5104.41	3536.78	30.71
13,000		3		3057.71	1938.19	36.61
12,500		4		3064.73	1940.02	36.70
12,000		5		291.31	193.99	33.41
11,000		10		105.57	189.90	-79.3

Many samples exhibited high FRET efficiencies indicative of effective energy transfer – for instance, 39.20% at 20,000 μL/min with 100 μg/mL of secretome-derived EVs. For samples prepared with 10 μg/mL of secretome-derived EVs, high efficiency was maintained down to 13,000 μL/min, below which carrier-in-carrier formation appeared incomplete; with 100 μg/mL of secretome-derived EVs, efficient assembly was achieved at flow rates as low as 12,000 μL/min. This behavior is consistent with lipid availability: at low lipid concentrations, high flow rates are required for uniform SFN surface coverage, whereas higher lipid concentrations allow assembly at lower flow rates. In general, higher flow rates favored more robust carrier-in-carrier formation.

These findings also correlate with particle size data: as previously noted, the carrier-in-carrier samples displayed distinct size distributions compared to SFNs or secretome-derived EVs alone, particularly at 13,000, 15,000, and 20,000 μL/min, supporting the formation of carrier-in-carrier architectures at these flow conditions.

The ensemble FRET efficiency values in Table 4 also provide semi-quantitative information on coating completeness. In a polydisperse ensemble, uncoated SFNs contribute their full unquenched donor fluorescence, diluting the observed E% in proportion to their abundance. Assuming a single-particle FRET efficiency of ~60% for fully coated SFNs (conservative estimate for donor-acceptor

separation of ~5 nm, consistent with the Förster radius of the FITC/Nile red pair), the observed ensemble E% values of 26-39% imply that at least 43-65% of SFNs are in nanometric contact with secretome-derived EV membranes – a conservative lower bound, since partially coated SFNs also contribute partial quenching. These data indicate substantial EV-SFN association under the tested conditions, though direct single-particle quantification by two-color NTA would provide a more rigorous measure and remains an important goal for future work.

Finally, in the cellular uptake study, microfluidically engineered carrier-in-carrier systems were compared with uncoated SFNs to assess selective internalization by healthy and tumor cells. Uptake was quantified by fluorimetric analysis across all experimental conditions, as this approach allows robust statistical comparison across multiple cell types, EV sources, SFN/EV ratios, and concentrations. The uptake of all samples was concentration- and time-dependent (Figure 3A and 3B, respectively; $p<0.05$). For SFNs, internalization was significantly higher in fibroblasts and mesothelioma cells than in MSCs, reaching high levels but showing no selectivity for a particular cell type. This indicates that, in the absence of the EV coating, SFNs lack selective targeting ability, as expected. In contrast, coating with secretome-derived EVs modified the internalization pattern, conferring cell-type specificity (Figure 3C and D). For MSC-derived carrier-in-carriers (CCMSC), uptake was significantly higher in healthy cells (MSC and fibroblasts) than in tumor cells. In particular, MSCs showed the highest uptake for the 1:1 ratio (CCMSC1), while less balanced ratios (1:2 and 1:3; CCMSC2 and CCMSC3) resulted in reduced internalization. This finding suggests that an optimal ligand density is crucial for efficient receptor-ligand interactions, whereas deviations may lead to steric hindrance or aggregation, thereby reducing recognition and uptake efficiency. In fibroblasts, no significant differences were observed among CCMSC1, CCMSC2, and CCMSC3, indicating that uptake is influenced by both the carrier's physicochemical characteristics and the specific cell phenotype. Conversely, in tumor cells, the opposite trend was observed: uptake was minimal for MSC-derived carrier-in-carriers – significantly lower than for SFNs, likely reflecting the absence of specific recognition motifs for mesothelioma surface receptors – while it was maximal for tumor-derived carrier-in-carriers, consistent with preferential homologous uptake mediated by mesothelioma-specific secretome-derived EV surface proteins. The source-dependent reversal of the uptake preference – MSC-secretome-derived EVs favoring healthy cells, mesothelioma-secretome-derived EVs favoring tumor cells – strongly suggests that the observed differential internalization reflects genuine biological recognition rather than non-specific variation in endocytic activity, consistent with the framework proposed by Muhandiram & Fazeli [15], who distinguish between EV uptake specificity and functional specificity.

Proteomic data from previous publications of our group allow us to propose specific molecular candidates underlying this cell-type-specific recognition. For mesothelioma-secretome-derived EVs, the proteomic characterization reported in Pinton et al. [58] identified several surface-associated proteins directly relevant to homologous tumor targeting. Mesothelin (MSLN, FC=2 relative to untreated controls) is a GPI-anchored glycoprotein highly expressed on mesothelioma cell surfaces that mediates cell-cell adhesion through interaction with MUC16/CA125 [65]; its presence on EV membranes would be expected to facilitate docking and preferential uptake by MSLN-expressing mesothelioma cells. Inter-alpha-trypsin inhibitor heavy chains H2 and H4 (ITIH2, ITIH4) participate in hyaluronan-mediated ECM organization and contribute to tumor microenvironment remodeling [66], potentially facilitating EV retention in the tumor milieu; SPARC modulates cell-matrix interactions [67] and may influence EV-cell contact efficiency; TIMP-2 regulates MMP activity at the cell surface and participates in integrin-mediated outside-in signaling [68]. Collectively, these proteins suggest a cooperative targeting mechanism in which integrin-dependent internalization – the primary driver of EV organotropism as established by Hoshino et al. [69] and Fuentes et al. [70] – is reinforced by tumor-specific adhesion modules present on the mesothelioma EV surface, creating a dual-recognition system that selectively favors uptake by homologous tumor cells over healthy counterparts. For MSC-secretome-derived EVs, the lyosecretome proteome characterized in Bari et al. [54] is enriched in ECM-associated and adhesion proteins, including fibronectin (FN1), multiple collagen chains (COL6A1, COL6A2, COL6A3, COL1A1, COL1A2), SPARC, TIMP1, TIMP2, thrombospondin-1 (THBS1), and vitronectin (VTN) – well-established ligands for integrins preferentially expressed on mesenchymal and stromal cells. Fibronectin engages α5β1 and αvβ3 integrins [71]; vitronectin and thrombospondin-1 are canonical αvβ3 ligands [72]; collagen chains are recognized by α1β1 and α2β1 integrins [73]. MSCs and fibroblasts – the healthy cell types showing preferential CCMSC uptake in our study – constitutively express these integrin repertoires as part of their mesenchymal identity. We acknowledge that these mechanistic proposals are inferential, derived from proteomic profiles of the EV source cells rather than from direct functional experiments on the carrier-in-carrier systems themselves; formal demonstration of receptor-mediated internalization would require competition assays with integrin-blocking antibodies, receptor knockdown or knockout approaches, and low-temperature uptake experiments to distinguish active endocytosis from passive membrane fusion. The observed selectivity – while mechanistically inferred rather than proven at the molecular level – is nonetheless functionally robust, as demonstrated by the consistent and statistically significant differential uptake pattern across three SFN/EV ratios and two EV sources.

While the present study does not include a direct assessment of therapeutic efficacy, the translational significance of the observed uptake selectivity is supported by prior work from our group

demonstrating that internalization of drug-loaded SFNs translates into functional intracellular cargo delivery and cytotoxic activity. For example, Pirota et al. [74] showed that cRGD-functionalized SFNs loaded with a potent naphthalene diimide (NDI) derivative achieved selective tumor cell killing through integrin-mediated uptake in cancer cells overexpressing αvβ3/αvβ5 integrins, demonstrating that SFN internalization is coupled to effective intracellular drug release and biological activity. Similarly, Bari et al. [30] demonstrated uptake-dependent functional delivery of an immunogenic cargo from SFNs in a cancer immunotherapy context. In the present carrier-in-carrier system, the EV coating superimposes a layer of biological specificity onto this established SFN delivery mechanism: mesothelioma-derived EVs dramatically enhance uptake selectively in homologous tumor cells (Figure 3C), while simultaneously reducing internalization in healthy cells relative to uncoated SFNs. In the present carrier-in-carrier system, the secretome-derived EV coating superimposes a layer of biological specificity onto this established SFN delivery mechanism, providing a strong preclinical rationale for tumor-selective drug delivery with reduced off-target effects.

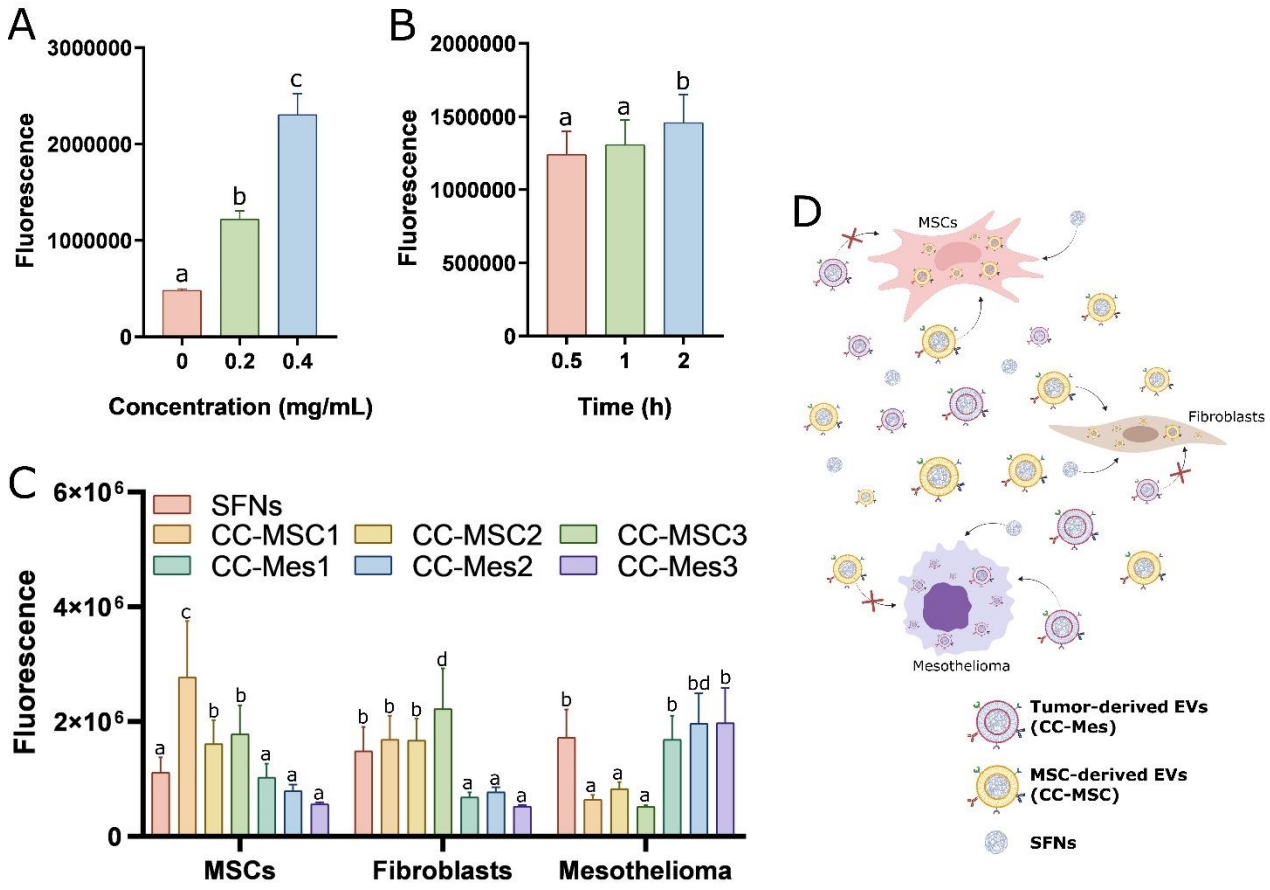

Figure 3. In vitro cell uptake to demonstrate cell-specificity of the carrier-in-carrier systems. (**A**) Cellular uptake as a function of the sample concentration. Multifactor ANOVA, mean ± standard deviation, n=3. (**B**) Cellular uptake as a function of the time of incubation. Data are reported as mean

± standard deviation; Multifactor ANOVA followed by LSD post-hoc, n=3. (**C**) Cellular fluorescence resulting from uptake of SFNs or microfluidically produced carrier-in-carriers prepared with MSC-secretome-derived EVs (CCMSC1, CCMSC2, CCMSC3) or mesothelioma-secretome-derived EVs (CCMes1, CCMes2, CCMes3) at SFN/EV ratios of 1:1, 1:2, and 1:3, respectively. Different letters indicate significant differences ($p<0.05$), while the same letter indicates non-significant differences ($p>0.05$). Data are reported as mean ± LSD; Multifactor ANOVA followed by LSD post-hoc, n=3. (**D**) Schematic representation of the selective uptake of carrier-in-carriers prepared using MSC- or mesothelioma-secretome-derived EVs.

4. Conclusions

This work demonstrates the development of a carrier-in-carrier system combining SFNs and secretome-derived EVs for targeted drug delivery. The EV coating enhanced colloidal stability, protected the encapsulated curcumin (used as a model lipophilic drug) from degradation, and enabled sustained, diffusion-controlled release. The sonication approach served as an essential proof-of-concept phase that validated the carrier-in-carrier architecture and its functional properties before translation to a GMP-compliant microfluidic process, which offers full parameter control, intrinsic scalability, and a wider accessible formulation space. NTA analysis confirmed the formation of uniform, stable complexes with tunable size distributions, while FRET assays verified nanoscale proximity between SFNs and secretome-derived EVs, confirming correct structural assembly. Finally, EV-coated carrier-in-carriers demonstrated precise, cell-type-specific uptake in vitro: MSC-secretome-derived EVs drove preferential internalization in healthy cells, whereas tumor-secretome-derived EVs promoted selective uptake in homologous tumor cells. The molecular basis for this selectivity is supported by proteomic evidence from previous characterizations of both EV sources, which identify ECM-binding proteins and mesenchymal integrin ligands in MSC-derived preparations and tumor-specific adhesion molecules – including mesothelin, ITIH2/H4, SPARC, and TIMP-2 – in mesothelioma-derived EVs; however, direct functional validation of these mechanisms through receptor-blocking or genetic approaches remains an important goal for future work. These results establish EV-based carriers as a versatile platform for precision oncology, maximizing therapeutic efficacy while minimizing off-target effects.

References

1. Zhao, Z.; Ukidve, A.; Kim, J.; Mitragotri, S. Targeting Strategies for Tissue-Specific Drug Delivery. *CELL* **2020**, *181*, 151-167, doi:10.1016/j.cell.2020.02.001.
2. Cirillo, M.; Giacomini, D. Molecular Delivery of Cytotoxic Agents via Integrin Activation. *CANCERS* **2021**, *13*, doi:10.3390/cancers13020299.

3. Roszkowski, S.; Durczynska, Z.; Szablewska, S. Targeted nanodelivery systems for personalized cancer therapy. *REPORTS OF PRACTICAL ONCOLOGY AND RADIOTHERAPY* **2024**, *29*, 776-788, doi:10.5603/rpor.103524.
4. Hristova-Panusheva, K.; Xenodochidis, C.; Georgieva, M.; Krasteva, N. Nanoparticle-Mediated Drug Delivery Systems for Precision Targeting in Oncology. *PHARMACEUTICALS* **2024**, *17*, doi:10.3390/ph17060677.
5. Kou, L.; Yao, Q.; Zhang, H.; Chu, M.; Bhutia, Y.; Chen, R.; Ganapathy, V. Transporter-Targeted Nanosized Vehicles for Enhanced and Site-Specific Drug Delivery. *CANCERS* **2020**, *12*, doi:10.3390/cancers12102837.
6. Zhang, W.; Kohane, D. Keeping Nanomedicine on Target. *NANO LETTERS* **2021**, *21*, 3-5, doi:10.1021/acs.nanolett.0c04638.
7. Welsh, J.; Goberdhan, D.; O'Driscoll, L.; Buzas, E.; Blenkiron, C.; Bussolati, B.; Cai, H.; Di Vizio, D.; Driedonks, T.; Erdbrügger, U.; et al. Minimal information for studies of extracellular vesicles (MISEV2023): From basic to advanced approaches. *JOURNAL OF EXTRACELLULAR VESICLES* **2024**, *13*, doi:10.1002/jev2.12404.
8. Kim, M.S.; Haney, M.J.; Zhao, Y.; Mahajan, V.; Deygen, I.; Klyachko, N.L.; Inskoe, E.; Piroyan, A.; Sokolsky, M.; Okolie, O.; et al. Development of exosome-encapsulated paclitaxel to overcome MDR in cancer cells. *Nanomedicine-Nanotechnology Biology and Medicine* **2016**, *12*, 655-664, doi:10.1016/j.nano.2015.10.012.
9. Cheng, P.; Wang, X.; Liu, Q.; Yang, T.; Qu, H.; Zhou, H. Extracellular vesicles mediate biological information delivery: A double-edged sword in cardiac remodeling after myocardial infarction. *FRONTIERS IN PHARMACOLOGY* **2023**, *14*, doi:10.3389/fphar.2023.1067992.
10. Macedo-da-Silva, J.; Santiago, V.; Rosa-Fernandes, L.; Marinho, C.; Palmisano, G. Protein glycosylation in extracellular vesicles: Structural characterization and biological functions. *MOLECULAR IMMUNOLOGY* **2021**, *135*, 226-246, doi:10.1016/j.molimm.2021.04.017.
11. Sánchez, G.; Bunn, K.; Pua, H.; Rafat, M. Extracellular vesicles: mediators of intercellular communication in tissue injury and disease. *CELL COMMUNICATION AND SIGNALING* **2021**, *19*, doi:10.1186/s12964-021-00787-y.
12. Liu, Y.; Wang, C. A review of the regulatory mechanisms of extracellular vesicles-mediated intercellular communication. *CELL COMMUNICATION AND SIGNALING* **2023**, *21*, doi:10.1186/s12964-023-01103-6.
13. Pascucci, L.; Cocce, V.; Bonomi, A.; Ami, D.; Ceccarelli, P.; Ciusani, E.; Vigano, L.; Locatelli, A.; Sisto, F.; Doglia, S.M.; et al. Paclitaxel is incorporated by mesenchymal stromal cells and released in exosomes that inhibit in vitro tumor growth: A new approach for drug delivery. *Journal of Controlled Release* **2014**, *192*, 262-270, doi:10.1016/j.jconrel.2014.07.042.
14. Peng, J.; Zhao, J.; Zhao, Y.; Wu, P.; Gou, L.; Fu, S.; Chen, P.; Lu, Y.; Yang, L. HeLa Cell-Derived Paclitaxel-Loaded Microparticles Efficiently Inhibit the Growth of Cervical Carcinoma. *International Journal of Nanomedicine* **2020**, *15*, 6409-6420, doi:10.2147/ijn.s246659.
15. Muhandiram, S.; Fazeli, A. Does extracellular vesicle specificity truly exist? *CELL COMMUNICATION AND SIGNALING* **2026**, *24*, doi:10.1186/s12964-026-02654-0.
16. Ha, D.; Yang, N.; Nadithe, V. Exosomes as therapeutic drug carriers and delivery vehicles across biological membranes: current perspectives and future challenges. *Acta Pharmaceutica Sinica B* **2016**, *6*, 287-296, doi:10.1016/j.apsb.2016.02.001.
17. Rufino-Ramos, D.; Albuquerque, P.R.; Carmona, V.; Perfeito, R.; Nobre, R.J.; de Almeida, L.P. Extracellular vesicles: Novel promising delivery systems for therapy of

brain diseases. *Journal of Controlled Release* **2017**, *262*, 247-258, doi:10.1016/j.jconrel.2017.07.001.
18. Han, Y.; Jones, T.; Dutta, S.; Zhu, Y.; Wang, X.; Narayanan, S.; Fagan, S.; Zhang, D. Overview and Update on Methods for Cargo Loading into Extracellular Vesicles. *PROCESSES* **2021**, *9*, doi:10.3390/pr9020356.
19. Carney, R. Raw data for: Orthogonal analysis reveals inconsistencies in cargo loading of extracellular vesicles. *Zenodo* **2024**, doi:10.5281/ZENODO.13274706.
20. Sivanantham, A.; Jin, Y. Impact of Storage Conditions on EV Integrity/Surface Markers and Cargos. *LIFE-BASEL* **2022**, *12*, doi:10.3390/life12050697.
21. Gelibter, S.; Marostica, G.; Mandelli, A.; Siciliani, S.; Podini, P.; Finardi, A.; Furlan, R. The impact of storage on extracellular vesicles: A systematic study. *JOURNAL OF EXTRACELLULAR VESICLES* **2022**, *11*, doi:10.1002/jev2.12162.
22. Klymiuk, M.; Balz, N.; Elashry, M.; Wenisch, S.; Arnhold, S. Effect of storage conditions on the quality of equine and canine mesenchymal stem cell derived nanoparticles including extracellular vesicles for research and therapy. *DISCOVER NANO* **2024**, *19*, doi:10.1186/s11671-024-04026-4.
23. Ahmadian, S.; Jafari, N.; Tamadon, A.; Ghaffarzadeh, A.; Rahbarghazi, R.; Mahdipour, M. Different storage and freezing protocols for extracellular vesicles: a systematic review. *STEM CELL RESEARCH & THERAPY* **2024**, *15*, doi:10.1186/s13287-024-04005-7.
24. Guimaraes, D.; Noro, J.; Silva, C.; Cavaco-Paulo, A.; Nogueira, E. Protective Effect of Saccharides on Freeze-Dried Liposomes Encapsulating Drugs. *FRONTIERS IN BIOENGINEERING AND BIOTECHNOLOGY* **2019**, *7*, doi:10.3389/fbioe.2019.00424.
25. Chen, C.; Sun, M.; Wang, J.; Su, L.; Lin, J.; Yan, X. Active cargo loading into extracellular vesicles: Highlights the heterogeneous encapsulation behaviour. *JOURNAL OF EXTRACELLULAR VESICLES* **2021**, *10*, doi:10.1002/jev2.12163.
26. Roerig, J.; Schulz-Siegmund, M. Standardization Approaches for Extracellular Vesicle Loading with Oligonucleotides and Biologics. *SMALL* **2023**, *19*, doi:10.1002/smll.202301763.
27. Meng, W.; He, C.; Hao, Y.; Wang, L.; Li, L.; Zhu, G. Prospects and challenges of extracellular vesicle-based drug delivery system: considering cell source. *DRUG DELIVERY* **2020**, *27*, 585-598, doi:10.1080/10717544.2020.1748758.
28. Mohak, S.; Fabian, Z. Extracellular Vesicles as Precision Delivery Systems for Biopharmaceuticals: Innovations, Challenges, and Therapeutic Potential. *PHARMACEUTICS* **2025**, *17*, doi:10.3390/pharmaceutics17050641.
29. Crivelli, B.; Perteghella, S.; Bari, E.; Sorrenti, M.; Tripodo, G.; Chlapanidas, T.; Torre, M.L. Silk nanoparticles: from inert supports to bioactive natural

carriers for drug delivery. *Soft Matter* **2017**, doi:DOI: 10.1039/C7SM01631J
30. Bari, E.; Ferrera, F.; Altosole, T.; Perteghella, S.; Mauri, P.; Rossi, R.; Passignani, G.; Mastracci, L.; Galati, M.; Astone, G.I.; et al. Trojan-horse silk fibroin nanocarriers loaded with a re-call antigen to redirect immunity against cancer. *Journal for immunotherapy of cancer* **2023**, *11*, doi:10.1136/jitc-2022-005916.
31. Bari, E.; Perteghella, S.; Torre, M.L. *Silk-based drug delivery systems*; Royal Society of Chemistry: 2020.
32. Bossi, A.; Bucciarelli, A.; Maniglio, D. Molecularly Imprinted Silk Fibroin Nanoparticles. *ACS APPLIED MATERIALS & INTERFACES* **2021**, *13*, 31431-31439, doi:10.1021/acsami.1c05405.

33. Matthew, S.; Seib, F. Silk Bioconjugates: From Chemistry and Concept to Application. *ACS BIOMATERIALS SCIENCE & ENGINEERING* **2023**, *10*, 12-28, doi:10.1021/acsbiomaterials.2c01116.
34. Farokhi, M.; Mottaghitalab, F.; Reis, R.; Ramakrishna, S.; Kundu, S. Functionalized silk fibroin nanofibers as drug carriers: Advantages and challenges. *JOURNAL OF CONTROLLED RELEASE* **2020**, *321*, 324-347, doi:10.1016/j.jconrel.2020.02.022.
35. Yoo, J.; Park, C.; Yi, G.; Lee, D.; Koo, H. Active Targeting Strategies Using Biological Ligands for Nanoparticle Drug Delivery Systems. *CANCERS* **2019**, *11*, doi:10.3390/cancers11050640.
36. Kaur, N.; Popli, P.; Tiwary, N.; Swami, R. Small molecules as cancer targeting ligands: Shifting the paradigm. *JOURNAL OF CONTROLLED RELEASE* **2023**, *355*, 417-433, doi:10.1016/j.jconrel.2023.01.032.
37. Yan, S.; Na, J.; Liu, X.; Wu, P. Different Targeting Ligands-Mediated Drug Delivery Systems for Tumor Therapy. *PHARMACEUTICS* **2024**, *16*, doi:10.3390/pharmaceutics16020248.
38. Bajracharya, R.; Song, J.; Patil, B.; Lee, S.; Noh, H.; Kim, D.; Kim, G.; Seo, S.; Park, J.; Jeong, S.; et al. Functional ligands for improving anticancer drug therapy: current status and applications to drug delivery systems. *DRUG DELIVERY* **2022**, *29*, 1959-1970, doi:10.1080/10717544.2022.2089296.
39. Yang, Q.; Parker, C.; McCallen, J.; Lai, S. Addressing challenges of heterogeneous tumor treatment through bispecific protein-mediated pretargeted drug delivery. *JOURNAL OF CONTROLLED RELEASE* **2015**, *220*, 715-726, doi:10.1016/j.jconrel.2015.09.040.
40. Zhu, L.; Jiang, M.; Wang, H.; Sun, H.; Zhu, J.; Zhao, W.; Fang, Q.; Yu, J.; Chen, P.; Wu, S.; et al. A narrative review of tumor heterogeneity and challenges to tumor drug therapy. *ANNALS OF TRANSLATIONAL MEDICINE* **2021**, *9*, doi:10.21037/atm-21-1948.
41. Cheng, X.; Chen, H. Tumor heterogeneity and resistance to EGFR-targeted therapy in advanced nonsmall cell lung cancer: challenges and perspectives. *ONCOTARGETS AND THERAPY* **2014**, *7*, 1689-1704, doi:10.2147/OTT.S66502.
42. Fu, Y.; Liang, S.; Luo, M.; Wang, X. Intratumoral heterogeneity and drug resistance in cancer. *CANCER CELL INTERNATIONAL* **2025**, *25*, doi:10.1186/s12935-025-03734-w.
43. Median, A.; Wheeler, H.; Jones, R.; Dolan, M. Relating human genetic variation to variation in drug responses. *TRENDS IN GENETICS* **2012**, *28*, 487-495, doi:10.1016/j.tig.2012.06.008.
44. Ingelman-Sundberg, M. Genetic and environmental causes for interindividual variability in drug pharmacokinetics. In Proceedings of the OPTIMAL DOSE IDENTIFICATION, 2001-01-01, 2001; pp. 175-186.
45. Leete, J.; Zager, M.; Musante, C.; Shtylla, B.; Qiao, W. Sources of inter-individual variability leading to significant changes in anti-PD-1 and anti-PD-L1 efficacy identified in mouse tumor models using a QSP framework. *FRONTIERS IN PHARMACOLOGY* **2022**, *13*, doi:10.3389/fphar.2022.1056365.
46. Yang, R.; Niepel, M.; Mitchison, T.; Sorger, P. Dissecting Variability in Responses to Cancer Chemotherapy Through Systems Pharmacology. *CLINICAL PHARMACOLOGY & THERAPEUTICS* **2010**, *88*, 34-38, doi:10.1038/clpt.2010.96.
47. Wang, J.; Dzuricky, M.; Chilkoti, A. The Weak Link: Optimization of the Ligand-Nanoparticle Interface To Enhance Cancer Cell Targeting by Polymer Micelles. *NANO LETTERS* **2017**, *17*, 5995-6005, doi:10.1021/acs.nanolett.7b02225.
48. Wang, Q.; Li, Z.; Gong, Y.; Xiong, X. The effects of ligand distribution and density on the targeting properties of dual-targeting folate/biotin Pluronic F127/Poly (lactic acid)

polymersomes. *EUROPEAN JOURNAL OF PHARMACEUTICS AND BIOPHARMACEUTICS* **2025**, *206*, doi:10.1016/j.ejpb.2024.114598.
49. Woythe, L.; Porciani, D.; Harzing, T.; van Veen, S.; Burke, D.; Albertazzi, L. Valency and affinity control of aptamer-conjugated nanoparticles for selective cancer cell targeting. *JOURNAL OF CONTROLLED RELEASE* **2023**, *355*, 228-237, doi:10.1016/j.jconrel.2023.01.008.
50. Tassa, C.; Duffner, J.; Lewis, T.; Weissleder, R.; Schreiber, S.; Koehler, A.; Shaw, S. Binding Affinity and Kinetic Analysis of Targeted Small Molecule-Modified Nanoparticles. *BIOCONJUGATE CHEMISTRY* **2010**, *21*, 14-19, doi:10.1021/bc900438a.
51. Thomas, A.; Karakattu, S.; Cagle, J.; Hoskere, G. Malignant Pleural Mesothelioma Epidemiology in the United States From 2000 to 2016. *Cureus* **2021**, *13*, doi:10.7759/cureus.14605.
52. Robinson, B.M. Malignant pleural mesothelioma: an epidemiological perspective. *Annals of cardiothoracic surgery* **2012**, *1*, 491-496, doi:10.3978/j.issn.2225-319X.2012.11.04.
53. Abbott, D.M.; Bortolotto, C.; Benvenuti, S.; Lancia, A.; Filippi, A.R.; Stella, G.M. Malignant Pleural Mesothelioma: Genetic and Microenviromental Heterogeneity as an Unexpected Reading Frame and Therapeutic Challenge. *Cancers* **2020**, *12*, doi:10.3390/cancers12051186.
54. Bari, E.; Perteghella, S.; Di Silvestre, D.; Sorlini, M.; Catenacci, L.; Sorrenti, M.; Marrubini, G.; Rossi, R.; Tripodo, G.; Mauri, P.; et al. Pilot Production of Mesenchymal Stem/Stromal Freeze-Dried Secretome for Cell-Free Regenerative Nanomedicine: A Validated GMP-Compliant Process. *Cells* **2018**, *7*, doi:10.3390/cells7110190.
55. Mocchi, M.; Bari, E.; Marrubini, G.; Bonda, A.F.; Perteghella, S.; Tartara, F.; Cofano, F.; di Perna, G.; Giovannelli, L.; Mandracchia, D.; et al. Freeze-Dried Mesenchymal Stem Cell-Secretome Pharmaceuticalization: Optimization of Formulation and Manufacturing Process Robustness. *Pharmaceutics* **2021**, *13*, doi:10.3390/pharmaceutics13081129.
56. Yerneni, S.; Yalcintas, E.; Smith, J.; Averick, S.; Campbell, P.; Ozdoganlar, O. Skin-targeted delivery of extracellular vesicle-encapsulated curcumin using dissolvable microneedle arrays. *ACTA BIOMATERIALIA* **2022**, *149*, 198-212, doi:10.1016/j.actbio.2022.06.046.
57. Caccavo, D. An overview on the mathematical modeling of hydrogels' behavior for drug delivery systems. *International Journal of Pharmaceutics* **2019**, *560*, 175-190, doi:10.1016/j.ijpharm.2019.01.076.
58. Pinton, G.; Bari, E.; Fallarini, S.; Gigliotti, V.; De Giorgis, V.; Chiazza, F.; Torre, M.L.; Manfredi, M.; Moro, L. EZH2 Inhibition in Mesothelioma Cells Increases the Release of Extracellular Vesicles That Skew Neutrophils Toward a Protumor Phenotype. *International Journal of Molecular Sciences* **2025**, *26*, doi:10.3390/ijms262110328.
59. Sancho-Albero, M.; Encabo-Berzosa, M.; Beltrán-Visiedo, M.; Fernández-Messina, L.; Sebastián, V.; Sánchez-Madrid, F.; Arruebo, M.; Santamaría, J.; Martín-Duque, P. Efficient encapsulation of theranostic nanoparticles in cell-derived exosomes: leveraging the exosomal biogenesis pathway to obtain hollow gold nanoparticle-hybrids. *NANOSCALE* **2019**, *11*, 18825-18836, doi:10.1039/c9nr06183e.
60. Seib, F.P.; Jones, G.T.; Rnjak-Kovacina, J.; Lin, Y.; Kaplan, D.L. pH-Dependent Anticancer Drug Release from Silk Nanoparticles. *Advanced Healthcare Materials* **2013**, *2*, 1606-1611, doi:10.1002/adhm.201300034.
61. Sharma, S.; Bano, S.; Ghosh, A.S.; Mandal, M.; Kim, H.-W.; Dey, T.; Kundu, S.C. Silk fibroin nanoparticles support in vitro sustained antibiotic release and

osteogenesis on titanium surface. *Nanomedicine-Nanotechnology Biology and Medicine* **2016**, *12*, 1193-1204, doi:10.1016/j.nano.2015.12.385.
62. Zhang, Y.-Q.; Shen, W.-D.; Xiang, R.-L.; Zhuge, L.-J.; Gao, W.-J.; Wang, W.-B. Formation of silk fibroin nanoparticles in water-miscible organic solvent and their characterization. *Journal of Nanoparticle Research* **2007**, *9*, 885-900, doi:10.1007/s11051-006-9162-x.
63. Shen, L.; Ji, H. The pharmacology of curcumin: is it the degradation products? *TRENDS IN MOLECULAR MEDICINE* **2012**, *18*, 138-144, doi:10.1016/j.molmed.2012.01.004.
64. Wang, Y.; Pan, M.; Cheng, A.; Lin, L.; Ho, Y.; Hsieh, C.; Lin, J. Stability of curcumin in buffer solutions and characterization of its degradation products. *JOURNAL OF PHARMACEUTICAL AND BIOMEDICAL ANALYSIS* **1997**, *15*, 1867-1876, doi:10.1016/S0731-7085(96)02024-9.
65. Rump, A.; Morikawa, Y.; Tanaka, M.; Minami, S.; Umesaki, N.; Takeuchi, M.; Miyajima, A. Binding of ovarian cancer antigen CA125/MUC16 to mesothelin mediates cell adhesion. *JOURNAL OF BIOLOGICAL CHEMISTRY* **2004**, *279*, 9190-9198, doi:10.1074/jbc.M312372200.
66. Shi, J.; Rose, M.; Heij, L.; Von Stillfried, S.; Cacchi, C.; Lurje, I.; Lurje, G.; Varambally, S.; Gaisa, N.; Jonigk, D.; et al. Characterization of ITIH6, a novel inter-α-inhibitor family member with prognostic significance in cholangiocarcinoma. *INTERNATIONAL JOURNAL OF BIOLOGICAL MACROMOLECULES* **2025**, *331*, doi:10.1016/j.ijbiomac.2025.148360.
67. Larson, J.; Yasmin, T.; Sens, D.; Zhou, X.; Sens, M.; Garrett, S.; Dunleyy, J.; Cao, L.; Somji, S. SPARC gene expression is repressed in human urothelial cells (UROtsa) exposed to or malignantly transformed by cadmium or arsenite. *TOXICOLOGY LETTERS* **2010**, *199*, 166-172, doi:10.1016/j.toxlet.2010.08.020.
68. Zucker, S.; Drews, M.; Conner, C.; Foda, H.; DeClerck, Y.; Langley, K.; Bahou, W.; Docherty, A.; Cao, J. Tissue inhibitor of metalloproteinase-2 (TIMP-2) binds to the catalytic domain of the cell surface receptor, membrane type 1 matrix metalloproteinase 1 (MT1-MMP). *JOURNAL OF BIOLOGICAL CHEMISTRY* **1998**, *273*, 1216-1222, doi:10.1074/jbc.273.2.1216.
69. Hoshino, A.; Costa-Silva, B.; Shen, T.L.; Rodrigues, G.; Hashimoto, A.; Mark, M.T.; Molina, H.; Kohsaka, S.; Di Giannatale, A.; Ceder, S.; et al. Tumour exosome integrins determine organotropic metastasis. *Nature* **2015**, *527*, 329-+, doi:10.1038/nature15756.
70. Fuentes, P.; Sesé, M.; Guijarro, P.; Emperador, M.; Sánchez-Redondo, S.; Peinado, H.; Hümmer, S.; Cajal, S. ITGB3-mediated uptake of small extracellular vesicles facilitates intercellular communication in breast cancer cells. *NATURE COMMUNICATIONS* **2020**, *11*, doi:10.1038/s41467-020-18081-9.
71. Su, Y.; Iacob, R.; Li, J.; Engen, J.; Springer, T. Dynamics of integrin α5β1, fibronectin, and their complex reveal sites of interaction and conformational change. *JOURNAL OF BIOLOGICAL CHEMISTRY* **2022**, *298*, doi:10.1016/j.jbc.2022.102323.
72. ‡, D.B.S.e.t.b.m.m.u.e.L.L.S.B.F.H. Distinct Ligand binding Modes for Integrin Mediated Adhesion to Fibronectinversus Vitronectin. *GLYCOBIOLOGY AND EXTRACELLULAR MATRICES* **2001**.
73. Chin, Y.; Headey, S.; Mohanty, B.; Emsley, J.; Simpson, J.; Scanlon, M. Assignments of human integrin α1I domain in the apo and Mg2+ bound states. *BIOMOLECULAR NMR ASSIGNMENTS* **2014**, *8*, 117-121, doi:10.1007/s12104-013-9465-7.
74. Pirota, V.; Bisbano, G.; Serra, M.; Torre, M.L.; Doria, F.; Bari, E.; Paolillo, M. cRGD-Functionalized Silk Fibroin Nanoparticles: A Strategy for Cancer Treatment with a

Potent Unselective Naphthalene Diimide Derivative *Cancers* **2023**, *15*, 1725, doi:https://doi.org/10.3390/ cancers15061725

The data supporting the findings of this study are available from the corresponding author upon reasonable request.